POLITECNICO
MILANO 1863

Scuola di ingegneria industriale e dell'informazione

Materials and nanotechnology engineering

Properties of Binder Jetting 3D Printed 316L Stainless Steel

Relatrice: Nora Francesca Maria Lecis

Co-Relatore: Massimiliano Bestetti

Giammarco Pazzucconi 927961

anno accademico 2020/2021

INDEX

FIGURES INDEX

TABLES INDEX

GRAPHS INDEX

ABSTRACT (Eng)

In recent years, developments in the field of Additive Manufacturing techniques have been exponential, by showing interesting advantages for various sectors, from the wide variety of materials to high geometric freedom, less waste of material and speed of realization. For metals, the most developed technologies were powder bed techniques, mainly fusion-based, where the final structure is consolidated by laser or electron beam. With these techniques, an excellent definition of shape and density close to the traditional metal is achieved. In Binder Jetting, on the other hand, it is the deposition of drops of liquid binder that allows the dust particles to be joined layer by layer, similar to a 3-D print. The pieces produced must then undergo a debinding and sintering process to reach the final density. Most of the research has been done in perfecting the process parameters to ensure the mechanical properties, but little was done in the field of corrosion behavior.

In this thesis, the effects of different process and thermal parameters on the porosity and mechanical properties, and the corrosion resistance of Binder Jetting AISI 316L stainless steel, are evaluated. The effect of layer thickness and binder saturation, and debinding and sintering atmospheres referring to the post-processing stages, were investigated via microstructural and compositional analysis and mechanical characterization. The effects of different printing parameters and a comparison with samples produced with traditional metallurgical techniques, has been analyzed for corrosion behavior. Two typical phenomena of austenitic stainless steels were tested: intergranular corrosion and pitting. For intergranular and generalized corrosion, a weight loss test was used. For resistance to pitting, electrochemical tests of linear and cyclic polarization were carried out. The results were also evaluated using SEM images and EDX analysis. The 316L steel produced in this work by Binder Jetting exhibited a fine equiaxed microstructure, tensile strength values comparable to those of cast products and superior ductility compared to other additive techniques. Binder Jetting Steel has also higher intergranular resistance and comparable pitting resistance compared to cast 316L.

SOMMARIO (Ita)

Negli ultimi decenni gli sviluppi nel campo delle tecniche di Additive Manufacturing sono stati esponenziali, mostrando interessanti vantaggi per diversi settori, dall'ampia varietà di materiali alla liberà geometrica della forma, minor spreco di materiale e velocità di realizzazione. Per i metalli, le tecnologie più sviluppate sono state quelle a letto di polveri, principalmente quelle a fusione, dove la struttura finale si consolida tramite laser o fascio elettronico. Con queste tecniche si raggiunge un'ottima definizione di forma e densità vicina al metallo tradizionale. Nel Binder Jetting invece, è la deposizione di gocce di legante liquido che permette di unire le particelle di polvere strato per strato, in maniera analoga a una stampa 3-D. I pezzi prodotti devono poi subire un processo di debinding e sinterizzazione, per raggiungere la densità finale. La maggior parte della ricerca è stata fatta nel perfezionamento dei parametri di processo per garantire le proprietà meccaniche, ma poco è stato fatto nell'ambito del comportamento corrosionistico.

In questa tesi vengono valutati gli effetti di diversi parametri di processo e della temperatura sulla porosità e le proprietà meccaniche, e la resistenza alla corrosione dell'acciaio inossidabile Binder Jetting AISI 316L. L'effetto del layer thickness e della saturazione del binder e l'atmosfera di debinding e sinterizzazione, relative alle fasi di post-elaborazione, sono stati studiati tramite analisi microstrutturali e compositive, oltre alla caratterizzazione meccanica. Per il comportamento a corrosione sono stati analizzati gli effetti di diversi parametri di stampa e fatto un confronto con campioni prodotti con tecniche metallurgiche tradizionali. Sono stati testati due fenomeni tipici degli acciai inossidabili austenitici: corrosione intergranulare e pitting. Per la corrosione intergranulare e generalizzata è stato utilizzato un test di perdita di peso. Per la resistenza al pitting sono state eseguite prove elettrochimiche di polarizzazione lineare e ciclica. I risultati sono stati valutati anche utilizzando immagini SEM e analisi EDX. L'acciaio 316L prodotto in questo lavoro da Binder Jetting ha mostrato una microstruttura equiassiale fine, valori di resistenza alla trazione paragonabili a quelli dei prodotti da fonderia e una duttilità superiore rispetto ad altre tecniche di additive manufactoring. Binder Jetting SS ha anche una maggiore resistenza intergranulare e una resistenza al pitting comparabile rispetto al 316L tradizionale.

1. Introduction

1.1 Additive manufacturing

Additive manufacturing (AM) is a recent field of manufacturing processes, indicating technologies based on the bottom-up creation of 3D objects. Its first application was for prototyping [1] [2], but it grew quickly to an all-purpose low scale production industry [3] [4]. This growth is due to many factors that set AM apart from classic manufacturing processes, such as the capability to create objects of otherwise impossible shapes directly form the CAD files.

The production has usually very few steps compared to the traditional methods, making the design extremely simple. In fact, it requires little more than the CAD project, which is already enough to start the main process [2]. AM is also easily manageable, with highly automated main process, which requires almost no set up and no assembly afterwards.

Having also low waste materials and high energy efficiency, AM technologies are perfect for small and medium scale production. Traditional manufacturing is rarely as efficient as AM, especially for smaller productions that are not worth the time to be optimized, while AM efficiency is independent on the production scale. [3] [5].

Another important factor in AM technologies is their flexibility. AM has a geometric freedom unachievable for classic manufacturing process, and has a great variety of usable materials (metals, ceramics, polymers [6]. Most of the techniques are material-specific: their key technology is used for a specific class of material. On the other hand, other techniques may be applied for different materials [6].

A peculiarity in metal AM technology is its microstructures, that are specific to their techniques. This may in theory be exploited, but for now it mostly gives an unpredictable or pour behaviour of the structure.

Looking at the entire range of materials available nowadays for AM, seven categories for AM technology are defined by the American Society for Testing and Materials (ASTM) [7].

- *Vat polymerization*, the oldest of the commercial AM processes, is based on the photolithographic crosslinking reaction of a liquid thermoset polymer resins to form a solid structure.
- *Binder Jetting* (BJ) processes deposit liquid in the form of droplets to bind powder material. The binder is adhesive and is ink-jetted onto the surface of a powder bed. Some form of post-processing to remove the binder and to densify the constituent powder is usually requested to achieve the final product.
- *Material extrusion* is a very widespread AM technology based on the low cost of the hardware. Feedstock is either forced through a nozzle or heated and melted prior to deposition. In other cases, the feedstock is deposited at room temperature, and a combination of solvent curing/drying and high-viscosity of the slurry is exploited to preserve part geometry.

- *Material jetting* is accomplished by depositing droplets of material onto a build platform. The feedstock is in most cases a photosensitive thermoset polymer, which is cured after deposition. This relies upon well-established inkjet technologies developed for conventional 2D printing.
- *Directed energy deposition* (DED) is a collection of processes that use focused thermal energy to melt and bind materials fed in powder or wire form. The thermal source is usually a laser or electron beam.
- *Powder Bed Fusion* (PBF) entails surface exposure of a powder bed to a heat source to enable binding. The heat source is typically a laser or electron beam, although intensive light sources have been used with physical or chemical "masks" to allow all voxels on an entire surface to be processed simultaneously. Powder bed fusion, due to the minimal constraints on feedstock type for manufacturing, is popular for part manufacture.
- *Sheet lamination* includes processes for which the feedstock is in form of sheets. Each sheet is either cut to shape, and then stacked/adhered to previous layers, or is bonded to the previous layer and then cut or hatched, to facilitate removal of the useless parts at the end of the build. [6] [8] [9] [10].

Focusing the analysis on processes used for metal, AM technologies include laminated object manufacturing, directed energy deposition (DED), stereo lithography appearance (SLA), selective laser sintering (SLS), selective laser melting (SLM), electron beam melting (EBM) and binder jet 3D printing (BJ3DP).

1.2 Powder Bed

Powder bed is one of the most important branches of additive manufacturing technologies. It is based on the deposition of subsequent layers of powdered material. Every layer will be partially fixed by polymer binder or localized fusion (and re-solidification), creating a section of the final object, so that the sum of all layers will result in the desired shape [11].

The powder bed techniques may be divided in two main categories: the Powder Bed Fusion and non-Fusion. Powder bed Fusion (PBF) is the most studied, and includes many well-known techniques such as Selective Laser Melting (SLM), Direct Metal Laser Sintering (DMLS) and Electron Beam Melting (EBM). These techniques are mainly focused on modeling metal by using a concentrated energy source to accurately fuse specific points of the powder layer. [12] Due to the small dimensions of the melted pools and the great cold mass surrounding them, solidification occurs extremely fast. This fact and the high amount of heat dispersed in the surrounding area, produces a peculiar non-equilibrium microstructure, which results in residual stresses and cracking. Additionally, products of oxidation can form particles that can be found as inclusion in the solidified microstructure. These brittle particles act as stress risers and are detrimental to mechanical properties [13].

One of the most important advantages in terms of microstructures is the minimal final porosity [14]. These techniques create almost full density objects, especially if compared to non-fusion powder bed, gaining higher mechanical properties and consequently more structural applications possibilities [15] [16].

1.3 Binder Jetting

Binder Jetting (BJ), also known as 3D printing (3DP), was developed at MIT in the early 1990s, and is part of powder bed technologies [17]. It is the only powder bed technique which does not rely on fusion to create the object. BJ consist in the deposition of layers of powder glued together by a polymeric binder [18] Figure 1.

1.3.1 BJ Features

BJ is very distinct form the others powder bed AM techniques [19]. It has the same geometrical advantages of all the powder bed techniques, having a temporary intrinsic support structure in the unused powder, but has many exclusive features not relying on fusion.

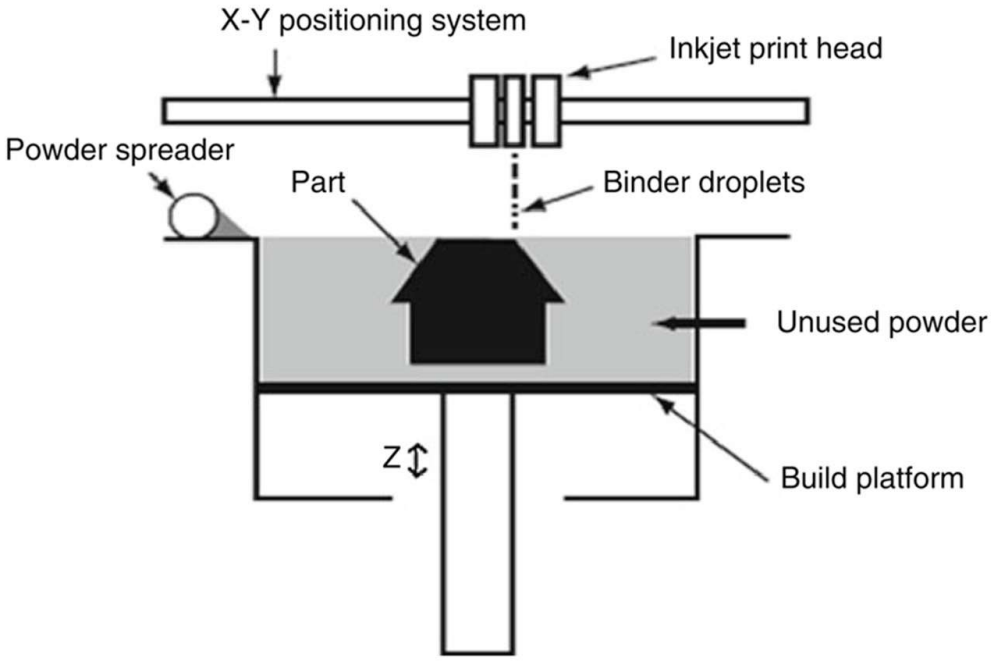

Figure 1 – Schematic representation of Binder Jetting process [18]

This difference is crucial, because operating at room temperature allows a higher freedom in the material choice, allowing the use of a wide variety of materials other than metals, such as ceramics, polymers, and more. It is worth noting that, since the printing process is almost identical for all materials, the same machine can operate with different kind of feedstock. Even if it is compatible with a wide range of materials, metals are the most widely used [11] [20] Furthermore, since BJ is mainly regarded as an offshoot of the other metal-based powder bed technique, the focus of researchers is mainly on post-printing processes, sintering in particular.

The main advantage of the lack of fusion is the possibility to have the basic metal phases/structure unchanged during the process. This prevents many undesirable side effects, such as residual stresses, heat affected zones (HAZ), oxidations, segregation, and phase changes.

There are many other advantages in being a heat free process, such as the lack of need of a protective atmosphere, which leads to a higher freedom for the machine chamber dimensions, allowing the creation of larger components. Also, the unused powders are completely reusable.

Since building up the object does not require fusion, the process is faster and has no need for a support material where to start its growth, being the powder itself self-sustaining [11].

To achieve a density comparable to the bulk material, infiltration could be used. For the stainless steel materials, bronze (a low melting alloy) is used as an infiltrant which can fill the open pores of the printed powder to improve the final density [21].

Being a powder bed technique, BJ is easily programmable with a CAD file for the object design. It is also especially easy to automate, having very few control parameters.

BJ product is still green, unusable as it is, which necessarily requires post processing in form of the debinding and sintering [11] [19]. This has some positive and negative effects. On the positive side, the densification of many sintered metals and ceramics is high enough to provide good mechanical properties [16]. Sintering also helps in achieving a controlled porosity, having higher control and finer pores [22] [23]. On the other hand, the need for extra steps is one of BJ shortcomings compared to other powder bed techniques, such as SLM. Other disadvantages deriving from sintering include lower detail resolution, rougher surface and shape distortions, caused by the great green porosity during the densification (shrinkage).

BJ, alongside with the two post-processes, is yet in need to be perfected and farther studied. At the moment, the studies were focused on the improvement of the densification, and the shape of the microstructure obtained at the end of the process, neglecting the study of mechanical, magnetic, and thermal characteristics. Very little has been studied of other non-metallic materials, despite BJ being the only powder bed techniques that may exploit them [19].

1.3.2 BJ Steps

Different steps are required to complete the full process in order to obtain a finite product.

The CAD project is analyzed by the BJ software, that slices the given 3D CAD file to 2D files corresponding to defined layer thickness.

1. *Printing*. As the print-head passes over a layer of powder, binder is deposited onto the powder. The job-box lowers, and a new layer of powder is deposited; the print-head passes again, depositing binder onto the second layer of powder. The binder is deposited layer by

layer by a set of nozzles, to create within the powder bed the shape of the final object (Figure 2).

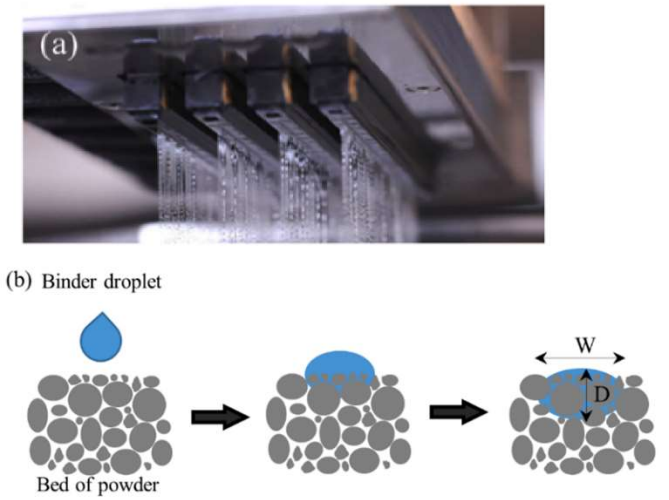

Figure 2 - (a) Printhead showing binder spraying and (b) binder droplet penetration in a bed of powder [19]

2. *Curing* at low temperature to promote the polymerization of the binder, improve the structural integrity of the component when still surrounded by loose powder [20].
3. *Depowdering* and extract the green body from the powder bed: complex geometries might require more careful steps then brushing the loose powder.
4. *Debinding* occurs during the initial stage of sintering, where binder becomes unstable and decomposes into constituents that can evaporate. For 316L parts, most of the binder phase usually burns out at approximately 450 °C.
5. *Sintering* at high temperature to achieve the densification of the component. Liquid phase sintering rather than solid state sintering gives better control on microstructure, less porosity in the sintered parts, and faster sintering at lower sintering temperature [11].

1.4 Austenitic stainless steel

1.4.1 Introduction

Stainless steels (SS)s are highly alloyed iron alloys, whose main purpose is to display a high corrosion resistance. Due to many applications in which this characteristic is required, such as chemical, petrochemical industry, food processing, pharmaceutical equipment, medical devices, potable water, wastewater treatment, marine applications, [24] SS are the most extensively used and researched steel alloy, with hundreds of different compositions. SS are the most extensively used and researched steel alloy, with hundreds of different compositions.

A good way to categorize these alloys is by their metallurgical phases. These are influenced by their alloying metals and so they also give a rough idea of their characteristics. This classification includes the following main categories: Austenitic, Duplex, Ferritic, and Martensitic SSs. The list starts from the tough and high corrosion resistance ones and continues with the harder and more fragile ones [25].

1.4.2 Alloying elements in SS

The corrosion resistance of SSs is achieved by exploiting the properties of chromium so to change the normal corrosion behavior of iron. By having a minimum Cr content of 11%, the steal will be considered a stainless steel, having a passive corrosion behavior. [25] [26]

Exceeded this threshold there will be a quick formation of a dense and adherent chromium oxide film whenever the alloy is exposed to an oxidizing environment (containing Oxygen). This passive layer prevents farther oxidation by denying the oxygen diffusion within the metal.

The other main component of austenitic steels is nickel. It is fundamental for duplex and austenitic SSs, such as the one used in this thesis, since its main use is to stabilize the austenitic (γ) phase. As additional advantage, it also provides a higher impact strength [25].

1.4.3 316L alloy

316L is the low carbon version of 316 stainless steel. The carbon reduction aims to reduce the precipitation of chromium carbide at intergranular inter-phases, thus avoiding chromium depletion, and maintaining effective corrosion resistance [27].

Alloy 316L is a well-known stainless-steel alloy and originated as improvement of the already remarkable corrosion resistance characteristics of 304 and 304L alloys. Through the addition of Molybdenum, there has been a significant increase of stability of the oxide layer. This results in a higher resistance to general corrosion and pitting, with also improvement of high temperature effects such as creep.

Composition for 316L (wt%):

Table 1 - Nominal composition of 316L stainless steel

Cr	Ni	Mo	C	Mn	P	S	Si	N	Fe
16-18	10-14	2-3	0.03	2	0.045	0.03	0.75	0.1	Bal

However, in spite of their name, stainless steel can be susceptible to pitting corrosion in aqueous environments, that allow micro structurally driven corrosion [28]. In austenitic stainless steels that are nominally single phase, such as 316L (Fe-Cr-Ni-Mo) or 304L (Fe-Cr-Ni), pitting corrosion events start in the vicinity of second-phase particles due to alloy impurities, such as manganese sulphide (MnS).

Austenitic stainless steels are typically prepared in either cast or wrought form, however AM has emerged as a technique to manufacture net shape SS components. In addition to the already mentioned advantages of the AM techniques (customization, freedom of design and ability to

manufacture complex parts), BJ3DP results in very pure phase composition, and the absence of inclusions is probably a major reason for the good pitting corrosion resistance [27].

1.5 Electrochemical test

Cyclic Potentiodynamic polarization Voltammetry (CPV) is an electrochemical test, a common practice for corrosion scientists, to study the active-passive behavior of alloys in contact with specific environments and highlight a variety of corrosion-related phenomena.

Usually, the typical approach to record an anodic polarization curve is based on the potentiodynamic method: using a three-electrode configuration cell, a linear potential-time ramp is applied between the working and the reference electrodes, and the current passing through the working and counter electrodes is measured [29].

The current density is then calculated, and the results of this test are given by a plot displaying the E vs log i curve (Graph 1).

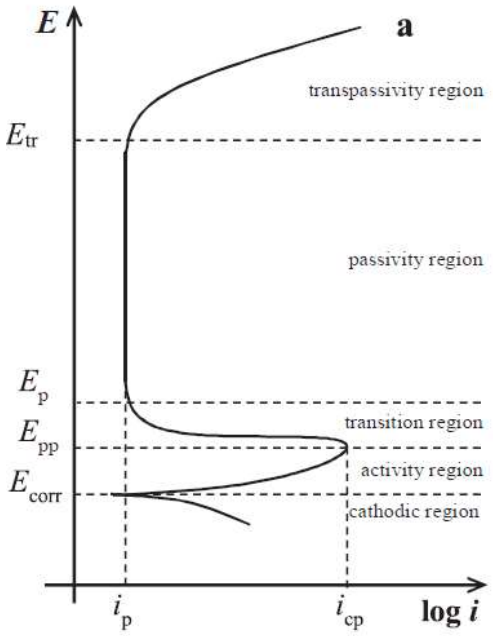

Graph 1 -Schematic representation of a generic anodic polarization curve [29].

The plot shows some characteristic parameters, which can be obtained from the curve:

- The critical current density of passivation i_{cp} and the corresponding primary passive potential Epp, where the passive film becomes stable and the transition of the alloy from the active to the passive state occurs.
- The passivation current i_p, where the anodic dissolution of the alloy undergoes a significant reduction from i_{cp}, bringing it to the condition of almost complete absence of corrosion.
- The passivation potential E_p, where the complete passivation starts.

- The transpassivation potential E_{tr}, which can be obtained in correspondence to an abrupt increase of current density during the scanning of potential. The increase of current density in correspondence of E_{tr} is determined by other anodic processes, such as the evolution of oxygen from water and/or the oxidation of other species as, for example, Cr III to Cr VI on SSs.

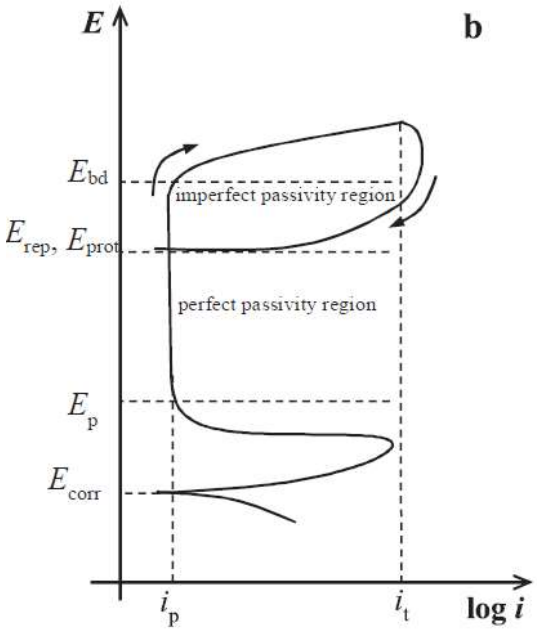

Graph 2 - In the presence of localized corrosion, cyclic potentiodynamic polarization curves are usually recorded, where two characteristic passivity regions are identifiable [29].

If the examined alloy undergoes localized corrosion, such as pitting, the passive film is damaged in correspondence to the breakdown potential E_{bd} (Graph 2), also known as pitting potential (E_{pit}). Generally, studying the localized corrosion, a cyclic potentiodynamic polarization (CPP) is planned by setting a current density threshold it (Figure 3) or a maximum potential Emax, where the potential is reversed toward more negative ones.

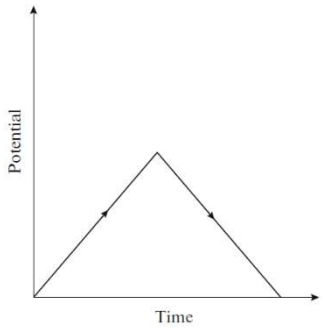

Figure 3 – potential during the test [30]

During the reverse scan, a negative hysteresis can be observed on the CPP curve: hysteresis is when the forward curve is not overlaid with the reverse scanning curve (Graph 2): the repassivation or protection potential (Erep or Eprot) can be determined in correspondence to the achievement of new passive conditions [30].

The amount of hysteresis, or the difference between $E_{pit} - E_{rp}$, indicates the amount of localized corrosion. If the current density in the reverse curve is more than the current density in the forward scanning curve, it will be indicative of pitting corrosion [30].

1.6 Scanning Electron Microscopy (SEM)

The electron microscope [31]does not use light as a source of radiation, but an electron beam, generated by an electronic source, typically a Tungsten filament. The flow of primary electrons is first accelerated by a potential difference of 0.3-30 kV, then concentrated by a series of electromagnetic lenses. The interaction between the electron and matter generates a signal, which is revealed and transformed into an electrical signal. This, treated and amplified, is modulated into a television signal: 1 pixel of a monochrome monitor is associated with 1 point of the sample and is the brighter the more intense the signal is. The magnification is given by the ratio between the size of the image and the size of the region on which it was scanned [32].

The result is a black and white image with high resolution and great depth of field.

The SEM must operate in high vacuum (with pressures below 10-3 Pa) and the samples must be conductive.

The interactions between electron and sample are read by special detectors. Depending on the nature, energy, and wavelength scattered, it is possible to obtain useful information for the analysis of the sample.

- The Everhart-Thorley detector allows the detection of secondary electrons. It is mounted in a tilted direction with respect to the beam and is characterized by a metal net on which a voltage of about 200V is applied. This allows to capture the secondary electrons and to conduct them in a channel, called light guide, where the energy of the electrons is transferred to photons, which are analyzed by a photomultiplier. The signal, once filtered and amplified, is brought to the monitor.
- The Back-Scattered Electron (BSE) detector allows the detection of backscattered electrons. They are mainly used in EDX (Energy Dispersive X-ray Analysis) spectroscopy or EDS (Energy Dispersive X-ray Spectrometry) spectroscopy. LA EDX is an instrumental analytical method that exploits the emission of X-rays generated by an accelerated electron beam incident on the sample, for the qualitative-quantitative characterization of metal alloys, in the context of materials science [32] [31].

2. State of the art

2.1 Corrosion Behavior of Binder-Jetted Metallic Speciment

Many aspects of the performance of 316L BJ3DP, including the corrosion behavior, are still not fully investigated [33] [11]. Articles in the literature focus on surface porosity, alloy addiction and printing direction in relation to corrosion resistance [34], or on surface finish of the printed pieces [27].

Very few works compare the behavior of BJ specimens, either with respect to traditional metal technique or SLM. At the present state, BJ specimens present a better corrosion profile then wrought specimens after immersion in acidic solution [27], while SLM specimens have similar behavior [35] [36] [37], although it may depend on other factors, such as scan speed, post-heating treatment, etc. [38], each of which can determine the characteristics of the single specimen [39].

The non-equilibrium microstructures that formed during LPBF/SLM manufacturing were regarded as the main reason for the reduced corrosion resistance [40].

The corrosion behavior in BJ can also be affected by the following steps of the process: debinding and sintering. Debinding [11] is essential to remove the binder (usually organic compound) before sintering, when the residual carbon may diffuse inside the steel, altering the nominal composition.

Due to the low green density of the binder jetted parts, high temperature sintering is necessary to achieve the desired final density. The sintering step [11] of the BJ3DP may play a major role in determine the final characteristics of the printed part. In in particular, time, temperature, and atmosphere composition of the process seem to affect the properties of the final product [22]. The sintering process is usually conducted at 1280 - 1370 °C for about 2 hours in pure Hydrogen or a Hydrogen/Argon atmosphere, for preventing oxidation.

Despite so many critical factors could affect the corrosion behavior of 316L BJ, up to now few works have been reported.

2.2 Aim of this work

The aim of this thesis is the assessment of mechanical properties and corrosion behavior of Binder Jetting 3-D Printed stainless steel specimens. Born for prototyping, Binder Jetting is a very promising technique for low scale, complex geometries products, in a variety of materials. Austenitic stainless steels are the most requested materials for countless applications, and their mechanical and corrosion properties were deeply investigated, also in additive manufacturing (as Selective Laser Melting), over the past few years [12]. On the other hand, studies about BJ are relatively scarce [11]. In the present research the effect of debinding and sintering parameters on the microstructure of a 316L stainless steel is described and effect of microstructural changes on bending strength, tensile properties, and micro-hardness is reported. It is also analyzed corrosion behavior of BJ 316L Steel, by means of intergranular corrosion analysis via a weight loss test in acidic environment, surface characterization, and the assessment of pitting susceptibility via electrochemical test.

3. Experimental methods

3.1 Feedstock powder

The feedstock powder used in this thesis was a gas atomized 316L stainless steel supplied by Sandvik AB with spherical shape (circularity$_{10}$ = 89%) and a unimodal particles size distribution (d_{10} = 2.1 µm, d_{50} = 3.8 µm, d_{90} = 7.8 µm). Chemical composition in Table 2.

Table 2 - Chemical composition by weight % of the powder used.

	C	O	Si	Cr	Mn	Fe	Ni	Mo
316L	0.03	0.21	0.58	18.28	2.19	65.73	10.90	2.12

3.2 Printing process

Printer used to produce all Binder Jetting samples of this study is an Innovent+ 3D BJ system by ExOne (Huntington, PA, US).

Figure 4 - ExOne Innovent® Plus 3D printer

The binder used during printing was a standard aqueous-based type BA-005 (1.069 g/cm^3) solution provided by ExOne. containing ethylene glycol monobutylether (EGBE), isopropanol (IPA), and ethylene glycol (EG). The first two constituents evaporate during the curing while the ethylene glycol cross-links producing PEG [41].

During this study two process parameters, layer thickness (LT) and binder saturation (BS), were selected to investigate the effects of their variation. LT was considered at two levels, 50 µm and 100 µm, whereas BS was set at 55% or 70%. Instead, all other printing parameters (Table 3) were kept fixed for all the samples here presented.

Table 3 - Constant printing parameters

Drying time *s*	Bed temperature *°C*	Recoat speed *mm s^{-1}*	Roller rotation speed *rpm*	Roller transverse speed *mm s^{-1}*
12	55	100.0	600	5.0

3.2.1 Types of Specimens

Using this technique, different types of specimens are created, varying in process parameters and shape.

1st type

Samples produced for 3-point bending tests and tensile tests were created in accordance with the ASTM standards B312-20 and E8/E8M, respectively. For tensile tests, three standard flat unmachined specimens for powder metallurgy were produced for each condition (central width = 5.7 mm), printed with the flat surface parallel to the powder layer (Figure 5).

Figure 5 – 1st type specimens for tensile testing.

2nd type

Samples were created with layer thickness of 50µm and with a binder concentration in the feeding of 55%. This samples were printed in shape of a square prism, with average height of 1.4mm, and side of 1cm. For simplicity, these specimens will be called “BJ 50-55” (Figure 6).

Figure 6 – 2nd type specimen for corrosion test

3rd type

This is a heterogeneous set of samples. with dimensions specified for each experiment (Figure 7). Different types are distinguished by combination of four different sets of process parameters. In Table 4, the printing parameters of the first and third type of samples, and their names, are listed.

Table 4 - Process parameters of first and third type binder jetting specimens

	Binder saturation	
Layer thickness	55%	70%
50 µm	BJ 1 or BJ 55BS 50LT	BJ 2 or BJ 70BS 50LT
100 µm	BJ 3 or BJ 55BS 100LT	BJ 4 or BJ 70BS 100LT

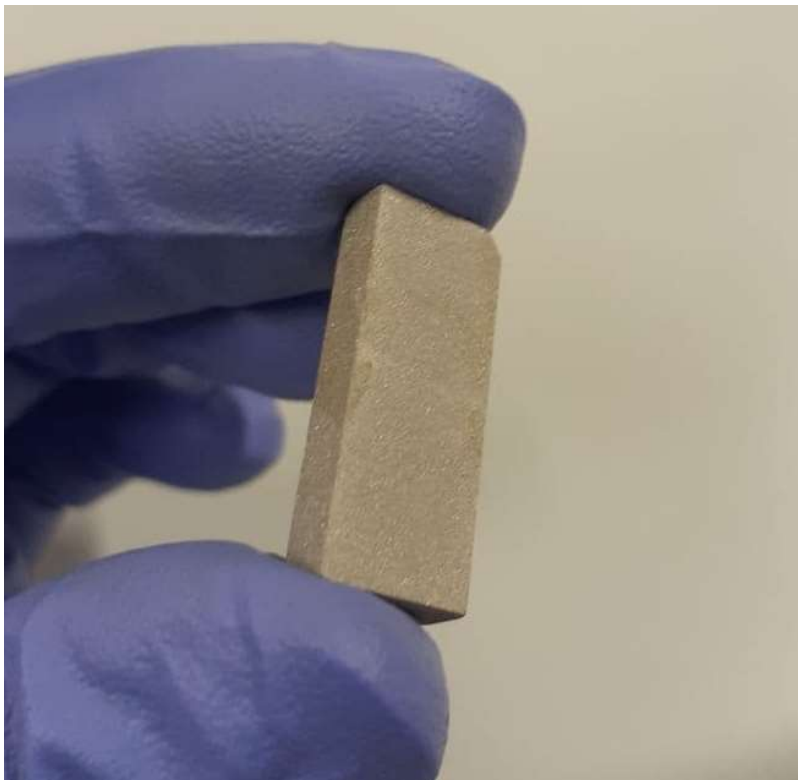

Figure 7 – Type two specimen for corrosion test

Comparison sample

To appreciate the corrosion behavior, BJ samples were compared with SS 316L samples, obtained from bulk material formed with traditional metallurgical techniques. The latter will be defined as standard (STD) specimens.

3.3 Curing, debinding and sintering process

The curing process was carried out at 180 °C in air, in a YAMATO DX 412 furnace, whereas the debinding step was performed in Ar atmosphere in a CARBOLITE 12/75/700 tube furnace at a temperature of 470 °C for 4 hours. Operating in a protective atmosphere prevents high temperature oxidation of the metal, however, it might also hinder its carbon extraction capability, compared to the pyrolysis in air of the traditional process.

The temperatures for the sintering cycle were based by BJ system manufacturer recommended cycle. Sintering was therefore performed in vacuum by using a HTS HT-S1 LPC vacuum furnace (10^{-1} mbar) at 1360°C for 3 hours, with a heating rate of 5 °C min^{-1}, followed by a cooling stage with a N_2 pressure of 1.5 bar and a rate of -500 °C min^{-1}. During sintering, samples were placed on alumina holders to avoid contamination from the support plate of the furnace.

3.4 Microstructural and mechanical characterization

3.4.1 SEM analysis

Microstructural observations were conducted by a field-emission scanning electron microscope (FE-SEM) ZEISS SIGMA 500 equipped by energy dispersive X-ray (EDX) detector by Oxford Inc. SEM investigations were performed on specimens after mirror polishing and chemical etching (H_2O:HCl:HNO_3 1:1:1, according to ASTM E407-07 standard) to study their microstructural properties, and on the fracture surfaces of tensile specimens to determine the failure mechanisms. The average grain size was determined by line-intercept method, according to the ASTM E112-13.

EDX analyses were conducted on polished surfaces to determine the elemental composition of the phases and inclusions identified in the samples.

For the surface analysis used for the 3rd corrosion experiment (STD, BJ1, BJ2, BJ3 and BJ4), no alterations were made to the specimens, while for the cross section they had to be polished. This happened through two metallographic preparations: grinding on papers with granulations of 120, 180, 240, 320, 600, 800, 1200, and 2500, in sequence, and finished with diamond paste of 6, 3 and 1μm.

Parameters used for SE and BSE imaging is 20kV and working distance was widely varied during general imaging.

3.4.2 Density

Sample density was derived by area fraction measurement acquired by image analyses on samples collected both at the green and sintered stages and by the Archimedes' principle (ASTM B962-17) on sintered samples only, since the open porosity of the green samples was excessively large to produce accurate estimates.

3.4.3 Linear shrinkage

Linear shrinkage was evaluated in the three different directions (X = Powder spreader axis, Y = Printhead movement axis, Z = Building direction axis) by measuring three bending test specimen size with a digital caliper after sintering.

3.4.4 Vickers hardness (HV)

Vickers hardness (HV) was measured by microhardness indentation (ASTM B933-20) on polished sectioned samples, close to their surface and in their central regions. The applied load was 100 g_f for a duration of 15 s. Data are obtained by averaging 10 measurements in different areas of the sintered samples. Transverse rupture strength was measured by three-point bending tests on both green (ASTM B312-20) and sintered (ASTM B528-16) specimens performed by an MTS SYNERGIE 200 testing frame at a loading rate of 90 N min^{-1}.

3.4.5 Tensile tests

Tensile tests were performed on standard flat test specimens for powder metallurgy products (ASTM E8/E8M) by an MTS ALLIANCE RT 100 testing frame, at a strain rate of 1.3 mm min^{-1}.

3.5 Corrosion characterization

3.5.1 Weight Loss Tests

The weight loss tests performed are based on the ASTM A262 (B) standard practice, commonly used for determining the susceptibility to grain boundary corrosion of austenitic stainless steels. According to the standard, samples should be immersed in a boiling solution of iron sulphate (Fe SO_4) and 50% sulfuric acid (H_2SO_4), a period ranging from 24 to 120h [42].

The experiments carried out in this study, are modifications of this practice. This was decided considering that second type specimens dissolve completely in a few hours, if immersed at high temperatures.

3.5.1.1 Experimental schedule

- 1st experiment

In this phase, a series of tests were performed to have a direct comparison between third type BJ specimens and standard specimens obtained from the bulk.

Third type samples have not undergone any treatment to change their surface and therefore they retain an as-sintered morphology. Standard ones were also not finished after being shaped.

The specimens were first degreased with an ultrasonic treatment in ethanol for 6 minutes. The samples were then dried and weighed using an analytical balance.

To create the acid bath, a 50% H_2SO_4 solution by weight was prepared. The specimens were immersed and left free to roam inside the solution, which is vigorously mixed by a magnetic stirrer. The acid attack was performed for 24 hours at room temperature. Even so, a condenser was used to make sure that the concentration is kept constant during the experiment.

Finally, the specimens are extracted and dried, and weighted again.

- 2nd experiment

This test aims to compare the results of samples with different BJ printing parameters.

Four samples were used and compared, one for each set of process parameters of the “third type samples”. (50-55, 100-55, 50-70, 100-70).

The preparation and procedure are the same as the previous test, with the samples exposing the surface resulting from the sintering process, which are degreased, soaked and extracted in 24 hours. The preparation and procedure are the same as the previous test: the samples have the as-sintered surfaces, the degreasing occurs with the same procedure, and with the samples being dipped in the acid bath for 24h.

In this case, however, all the specimens undergo a second corrosion test, that is performed with the same operative conditions of the first.

- 3rd experiment

This experiment has a similar purpose to the previous one, however it uses a different experimental design and takes in account the standard specimen, and not any other BJ.

The samples are initially uniformed by polishing the surface with 180, 320, 600 and 800 abrasive papers in sequence. They are then weighed directly, without the degreasing ultrasonic bath. The acid solution is identical, except for the specimens that are suspended with a Teflon thread, so to avoid constant collisions with the stirrer and each other.

Extracted after 24 hours, the samples are rinsed with water, and undergo an ultrasonic bath in water to detach the oxide layer present on the surface and within its roughness. The samples are then rinsed with water, ethanol, and acetone.

After being weighed, the samples are immersed again for a second bath. The extraction procedure is repeated after another 24 hours of immersion.

- 4th experiment

To estimate the evolution of corrosion with time, a test with different bath duration on BJ1 vs STD specimens was performed. This was also performed to investigate the different behavior exhibited in the second 24h bath between 2nd and 3rd experiment.

The procedure is basically the same of the third experiment, having the same solution, immersion method, preparation, and procedure after, changing only the duration of the bath. The experiment is performed once for each type of sample over 4 different times: 6, 12, 24 and 48 hours.

3.5.1.2 Weight Loss Assessment

In these tests, the progress of corrosion is measured through the loss of mass, which is evaluated as corrosion penetration after being converted.

To do such conversion, the following formula is used [42]:

$$\text{Penetration rate} = \frac{87660\ \Delta M}{A\ \rho\ t}$$

This formula assumes that as the exposed surface may be assumed constant throughout the entire process. The parameters inside are: lost mass ΔM [g], surface area A [cm^2], density of the material ρ [g/cm^3] and immersion time t [h]. Corrosion penetration is therefore measured in mm/year.

3.5.2 Electrochemical test: Cyclic potentiodynamic polarization

Samples of SS 316L and BJ3D steel were prepared by polishing and degreasing their exposed surface. The surface finishing has been obtained by emery papers up to 1200 grit. The samples will then be degreased with two ultrasonic baths in ethanol and acetone for 5 minutes each. The samples, exposing only a circular area of 1cm in diameter (Figure 8), are then used as working electrode in a standard three electrode cell, putting them in electric contact with the system. The other electrodes were a Pt counter electrode and a SCE reference electrode.

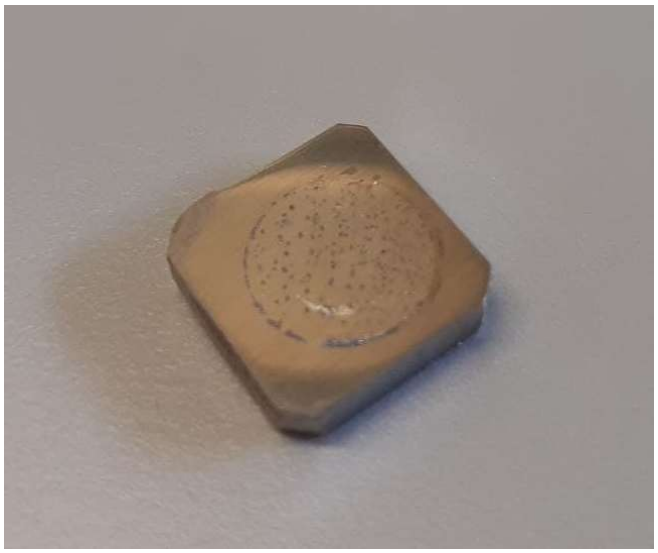

Figure 8 - specimen after the test, showing intended pitting on the exposed aera.

The exposed surface of the working electrodes was 0,7854 cm^2.

The testing acid solutions is at 1,6 pH, with 2,47g/l of concentrated HCl solution (about 37 wt.%).

Electrochemical tests were performed at room temperature (actually very high T, with temperatures around 30°C).

The potentiodynamic scans (0.50 mV /s) were carried out using an AMEL 2553 (IT) potentiostat. All anodic scans started from a potential more negative than free corrosion potential, which was initially measured in stationary conditions. The potential was increased up to a potential threshold (at 1200 mV vs SCE) and the scan was reversed in order to evaluate possible repassivation potential.

3.5.3 Roughness Evaluation

Given the clear change in the behavior shown by all the samples during the third experiment, it was decided to look for an indicator of the progress of corrosion. Surface roughness was than indagated, supposing that its measurements could relate to the current state of corrosion. The measurements were carried out on the specimens of the third experiment and on equivalent specimens, prepared and abraded with the same procedures used in the preparation of the first.

Measurements were taken in three different directions at 0 °, 45 ° and 90 °. The values reported are averages of these three directions.

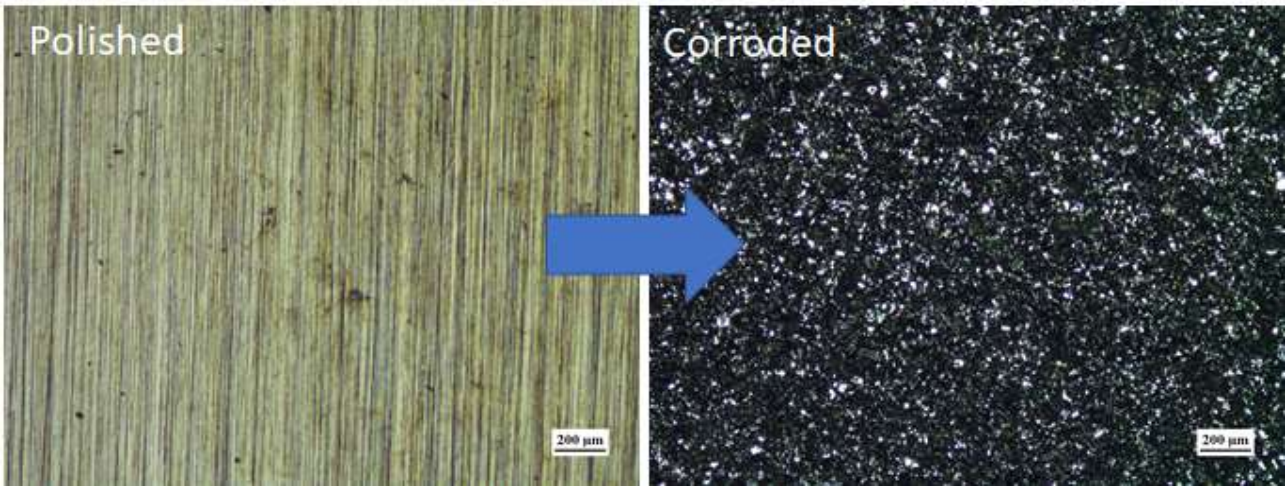

Figure 9 - Polished surface of BJ specimen before corrosion (left) and after 24 + 24 h in 50% H_2SO_4 solution (right).

The evaluation of the progressive change in surface roughness was made so to look for a possible correlation between surface topography and corrosion trend.

A pair of samples of each type (STD and BJ) were analyzed, one freshly polished with abrasive papers and the other after the corrosion of the third experiment (24 + 24h).

4. Results and discussion

4.1 Curing, Debinding and Sintering

As previously mentioned, the curing treatment was performed in air at 180 °C to induce a further reticulation of the binder and so the consolidation of the printed solid. Prior to sintering, a debinding heat treatment was performed at 470 °C for 4 hours in an Argon atmosphere, in order to yield a quantitative elimination of the binder. The binder must be efficiently removed, since residual carbonaceous species can lead to a carbon enrichment and to the precipitation of detrimental secondary phases that can modify the microstructure and performance of the final object. [43]

A previous research work in the group of Prof. Lecis was carried out to compare the effects of debinding in air and in argon atmospheres. The residual carbon analyses on samples debinded at 470 °C in the two atmospheres revealed that there is a large difference in the carbon concentration of the brown samples, namely after debinding, before sintering: 0.02 wt.% (air-debinded, which substantially corresponds to the original carbon content in the feedstock powder) and 0.13 wt.% (Ar-debinded). The complete burning of polymer is assured only for air-treated samples. [44]

Although debinding was not completed using an inert atmosphere, such option was preferred for the treatment of the testing samples for two main reasons:

-Oxidation of the metallic powder is prevented, thus favoring the following sintering and densification stages, and even allowing the use of vacuum sintering instead of a reducing atmosphere in the following thermal cycles.

-The residual binder after Ar-debinding should be about 0.02 wt.% thus its effect on the microstructure could be insignificant.

The sintering conditions were kept constant under investigation, with a holding temperature of 1360°C (reached by a heating rate of 5 °C min^{-1}) and a soaking time of 3 h under a vacuum atmosphere at 10^{-1} mbar. Vacuum sintering was preferred because low amount of residual oxides are expected after the Ar debinding, and it should prevent the formation of gas-filled closed pores, that would hinder full densification.

Sintering in vacuum [44], instead of using an in a hydrogen atmosphere, as required by the most standardized protocols, should help by avoiding the chance of hydrogen embrittlement, as well as reducing potential risks of using a flammable and potentially explosive gas at high temperatures. Vacuum sintering also results in better densification, since the absence of gas in the pores increases the pore shrinkage rate [22].

The increased amount of carbon has multiple effects on stability of phases. Firstly, it lowers the liquidus threshold from 1400 °C to about 1360 °C, potentially promoting the achievement of supersolidus liquid sintering. This might be an advantage since it accelerates diffusion and promotes the pore-filling effect, thus enhancing densification [45] [46]. Secondly, the larger C content may cause the stabilization of the austenite as opposed to the formation of δ-ferrite. This might influence sintering given its dependence on self-diffusion of iron, which is faster in the BCC structure of ferrite

than the more compact FCC lattice of austenite [47]. Regarding other compounds, an important advantage of the excess carbon is the reduction in the formation of the σ-phase, which is brittle, and it would worsen the mechanical performance of the material. Unfortunately, the increase in carbon is expected to lead to the formation of carbides (Mn23C6) [48]. This could raise the risk of intergranular corrosion and loss of toughness when comparing properties to those of more conventional wrought 316L steels [16].

4.2 Characterization of sintered samples

Table 5 summarizes the final sintered densities, shrinkage values for each axis and the grain sizes for each different as-sintered specimen, as reported from previous research work in the group of Prof. Lecis. Figure 10 illustrates the microstructure a polished cross-section of a 50-55BJ sample (BJ1). From Table 5, it can be noticed that there is a difference in density between samples printed with 50LT and 100LT. On the other hand, small density differences arise between samples with the same layer thickness but different binder saturations, in particular for the 100LT samples. This is likely due to the excess porosity in the inner region of the 70BS samples, possibly generated by the larger amount of binder that is removed during debinding. In addition, the 100LT70BS sample also displays a larger amount of unsintered particles, as shown in Figure 11.

Table 5 - Average value of relative density, shrinkage, grain size.

	55BS 50LT	70BS 50LT	55BS 100LT	70BS 100LT
Density / %	98.33 ± 0.02	97.66 ± 0.02	97.54 ± 0.04	95.78 ± 0.07
Shrinkage X / %	15.07 ± 0.74	14.13 ± 0.54	16.15 ± 0.17	14.77 ± 0.35
Shrinkage Y / %	15.75 ± 0.23	14.99 ± 0.04	16.96 ± 0.44	15.25 ± 0.45
Shrinkage Z / %	17.48 ± 0.45	16.48 ± 0.20	20.05 ± 0.97	17.59 ± 0.20
Grain size / µm	34.99 ± 3.77	37.82 ± 2.91	28.95 ± 2.63	33.10 ± 3.02

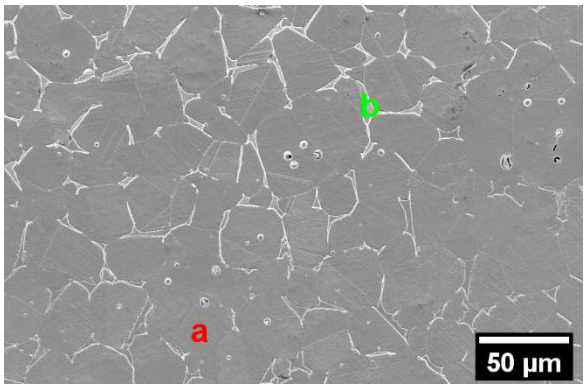

Figure 10 – SEM image of BJ (50 -55) surface after etching for EDX analysis.

Table 6 – EDX analisis of Figure 10.

Area	Phase	Si	Cr	Mn	Fe	Ni	Mo
a	γ	0.48	17.39	1.70	67.89	10.83	1.70
b	δ	0.53	24.01	1.56	64.61	5.33	3.83

As can be seen from the set of micrographs shown in Figure 11, internal porosity in all samples is extremely limited, characterized by a spherical shape, a size in the range 1-20 µm, and homogeneously distributed in the matrix, both inside grains and at grains boundaries. The small-size intragranular pores are extremely difficult to annihilate without pressure-aided sintering, thus the value of 99% relative density should be considered as a reasonable upper densification limit under these conditions [49] [50]. Densities near or above 99% have been achieved only with sintering aids [41] or with extensive liquid sintering [45]. Inclusions are rare or absent. In addition, the microstructure features equiaxed austenitic grains decorated by δ-ferrite (Figure 10), as suggested by EDX measurements reported in

Table 6 [51].

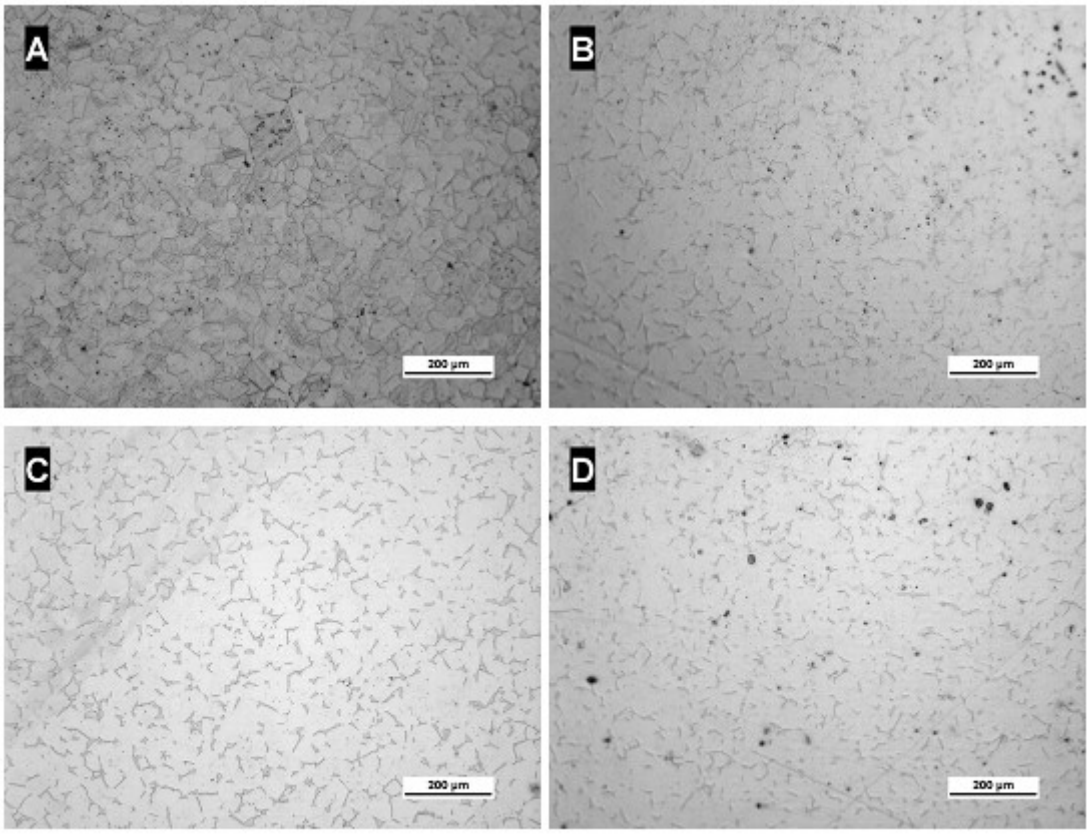

Figure 11 - Optical micrographs of samples: a) 55BS 50LT; b) 70BS 50LT; c) 55BS 100LT; d) 70BS 100LT after sintering

The linear shrinkage values, calculated in the three directions, confirm that the powder packing in the 100LT samples is lower, thus shrinkage is larger. In addition, it can be noticed that the shrinkage along the building direction is higher because of improper powder packing between layers [52] .

It can be noticed that the 50LT samples feature lower shrinkage and larger grain size. This might be explained by considering the competitive mechanisms of grain coarsening and material densification, dependent on pore size distribution. Therefore, two scenarios may be hypothesized as explanation of microstructure evolution:

- 50LT shows homogeneous distributions of small pores, due to high green packing, that are easily annihilated right at the onset of the sintering, thus promoting densification and earlier grain growth.

- 100LT shows wider pore size distribution including macro-voids and experiences the fast closure of the small pore fraction. However, the persistent presence of the larger voids (Figure 11b) hinders grain coarsening. Consequently, shrinkage at the end of the process can become larger, assuming macropores can eventually be annihilated.

The variation of the binder saturation seems to affect mainly the grain growth, rather than the shrinkage. It can be considered that the presence of the liquid phase (promoted by a higher carbon content) drastically enhances the diffusion process, thus favoring grain coarsening [46]. However, in the present investigation, the measured grain growth was not excessive, considering that the grain size is only 3-4 times larger than the coarser powder particles (d_{90}). An additional effect that can be observed in Figure 10, is the formation of grain boundaries with rounded profile that better accommodate the liquid phase and are typical of this type of sintering [53].

4.3 Micro hardness

The average microhardness values and the standard deviations are summarized in Table 7. Overall, the values measured are proportional to the grain size of the corresponding printing conditions, coherently with the Hall-Petch strengthening mechanism.

Table 7 – average value of Vickers hardness

Sample	Vickers Hardness (HV)
55BS 50LT	150 ± 9
55BS 100LT	164 ± 14
70BS 50LT	148 ± 11
70BS 100LT	150 ± 12

These results are comparable to literature data [41] about 316L BJ. The same steel, processed with other Laser-based AM technologies usually features much higher values due to the extremely refined microstructure [54].

4.4 Tensile properties

The results of the tensile tests, as previous research work in the group of Prof. Lecis, are displayed in Figure 12 while the main tensile data are summarized in Table 8 and compared with properties of the 316L steel processed by other methods. A large ductility is obtained for all the BJ specimens here investigated, regardless of the printing conditions.

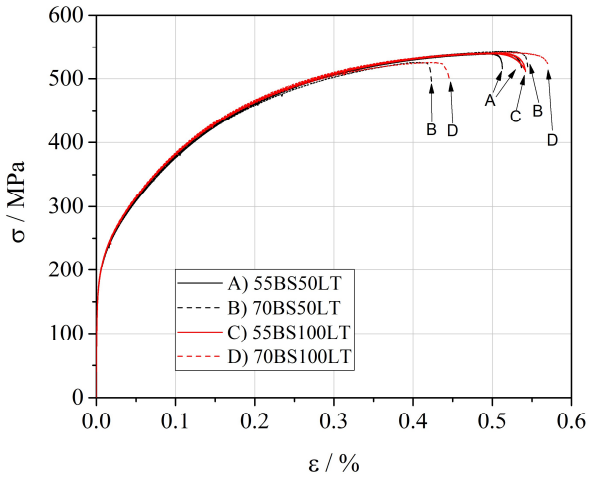

Figure 12 - Best and worst performance stress vs. strain curves obtained from the tensile tests

Table 8 – Tensile result of BJ samples compared with metal injection molding (MIM), Laser-powder bed fusion (L-PBF) and standard annealed cast bar from ASTM A276/A276M - 17 standard.

	0.2%YS	UTS	ε_{max}
	MPa	*MPa*	*%*
55BS 50LT	175 ± 1	540 ± 1	53 ± 1
55BS 100LT	175 ± 3	540 ± 1	55 ± 1
70BS 50LT	176 ± 1	535 ± 9	49 ± 7
70BS 100LT	174 ± 1	534 ± 8	51 ± 7
MIM [55]	~200	410 ± 18	22 ± 1
L-PBF [56]	554 ± 5	685 ± 5	36 ± 2
L-PBF [57]	423 ± 3	695 ± 3	41 ± 2
Cast 316L [58]	310	620	50

The material features a similar mechanical behavior with respect to cast steel, although the yield and tensile strengths are lower. The absence of a preferred crystal orientation, of coarse pores and low inclusion content allowed to achieve fairly good combination of mechanical strength and ductility.

Differences among the four printing parameter combinations are minimal. The main difference stands in the variability of fracture elongation values, and consequently of the UTS achieved, which might be due to the statistical effects of occasional pores and inclusions (Figure 13), that could trigger the onset of ductile fracture process. However, it can reasonably be claimed that all the investigated conditions provided a comparable behavior in the elastic and elasto-plastic regimes of the tensile curves, up to at least a strain of 40%.

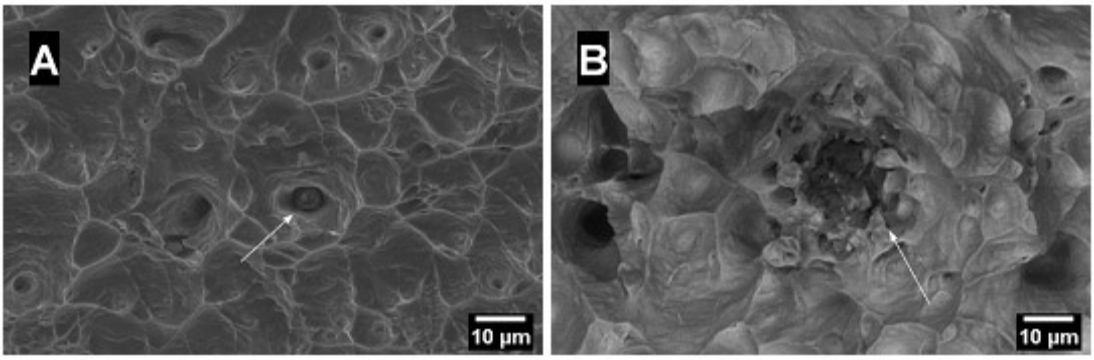

Figure 13 - SEM images of a rounded Cr-Mn-oxide inclusion (a) and an irregular micro-void likely produced by a brittle phase (b)

The typical features of ductile materials have been observed on the fracture surface of all the samples tested (Figure 14a). In few specific cases, microvoids may have nucleated from the rare inclusions and brittle phases that can be found in some samples, particularly those with higher binder saturation, as reported in Figure 13. However, the presence of these detrimental phases is so low that effects on the overall mechanical behavior of the samples was not observed. Indeed, most of the larger voids have likely formed from pre-existing porosity, as show in Figure 14b.

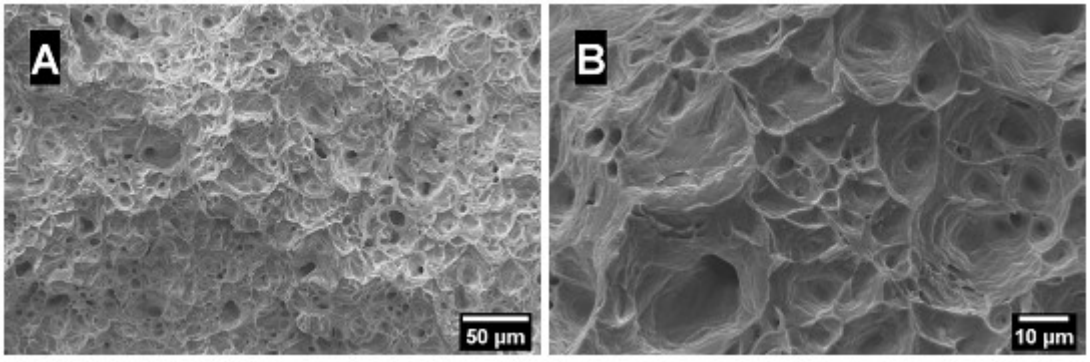

Figure 14 - SEM images of the fracture surface of the tensile specimens at different magnifications

4.5 Weight Loss tests

The results and considerations presented in this chapter are focused on the comparison between the bulk metal product (STD) and the BJ one.

4.5.1 1st Experiment

There is a clear distinction between the penetration rate of the two groups of specimens, with the Binder Jets showing a much higher corrosion resistance than the standard.

This is true for all results except the first, with obviously anomalous behavior. Graph 3 and Table 9.

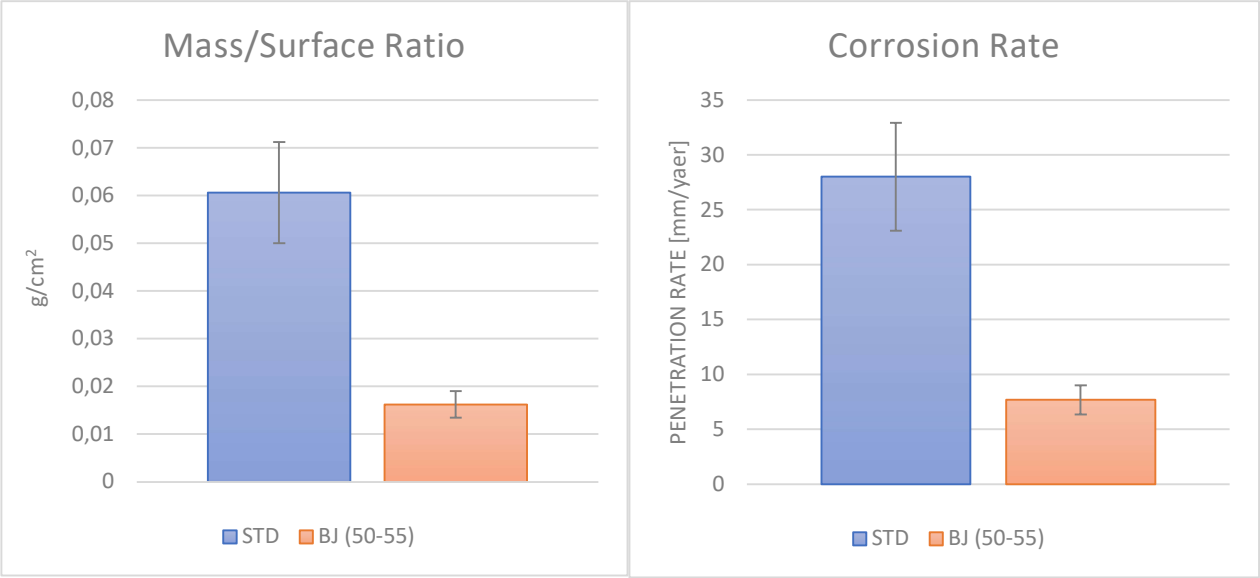

Graph 3 – Average and standard deviation of 1st experiment STD and BJ (50-55) samples

Table 9– Experiment n.1 – Corrosion data (average)

Type of Speciment	Δ Mass / Surface Ratio [g/cm^2]	Penetration Rate [mm/yaer]
STD	0,061 ± 0,011	28,0 ± 4,9
BJ (50-55)	0,016 ± 0,003	7,7 ± 1,3

4.5.2 2nd Experiment

In this test it does not appear to be a clear difference between the various specimen types.

It is also necessary to take into account the unreliability of the results of this test, as there was an intense exfoliation of the samples, probably due to the repeated collisions among themselves. Graph 4 and Table 10.

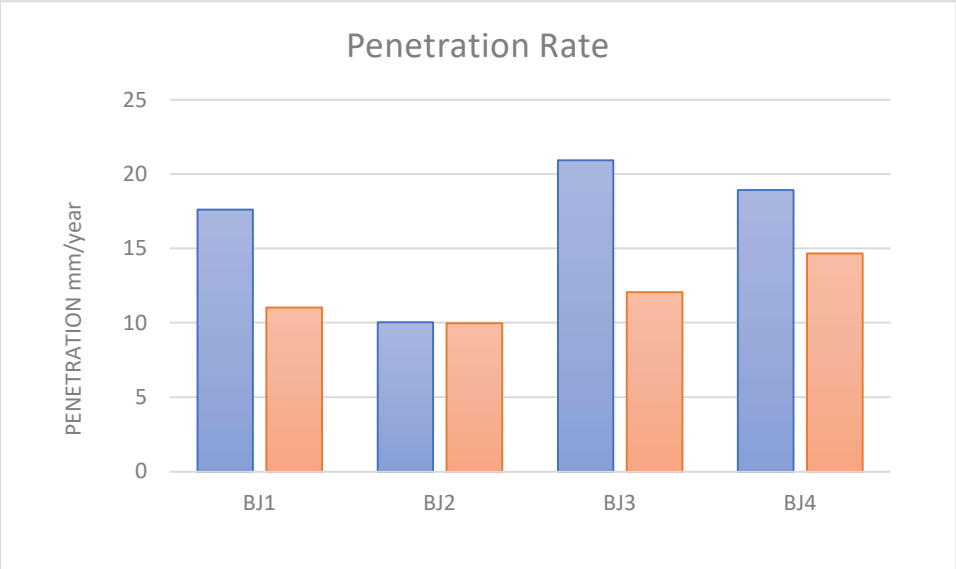

Graph 4– Experiment n.2 - Corrosion 24-48h

Table 10– Experiment n.2 - Corrosion 24-48h

Type of Speciment	Δ Mass / Surface Ratio [g/cm^2]		Penetration Rate [mm/year]	
Time	0-24h	24-48h	0-24h	24-48h
BJ1 - 55BS 50LT	0,037	0,019	17,625	11,029
BJ2 - 70BS 50LT	0,021	0,018	10,034	9,969
BJ3-55BS 100LT	0,044	0,023	20,935	12,073
BJ4 -70BS 100LT	0,039	0,026	18,939	14,663

4.5.3 3rd Experiment

In this experiment the test was performed three times, in order to obtain a more significant set of data. In Graph 5 are shown the first 24h results for each test in which is confirmed the difference in the corrosion resistance of the metal from BJ compared to the standard. In Graph 6 and Table 11 (expressed as average and standard deviation of the three tests) is instead evident a lack of corrosion in the second dive, due to the change of the experimental conditions from the 2nd experiment.

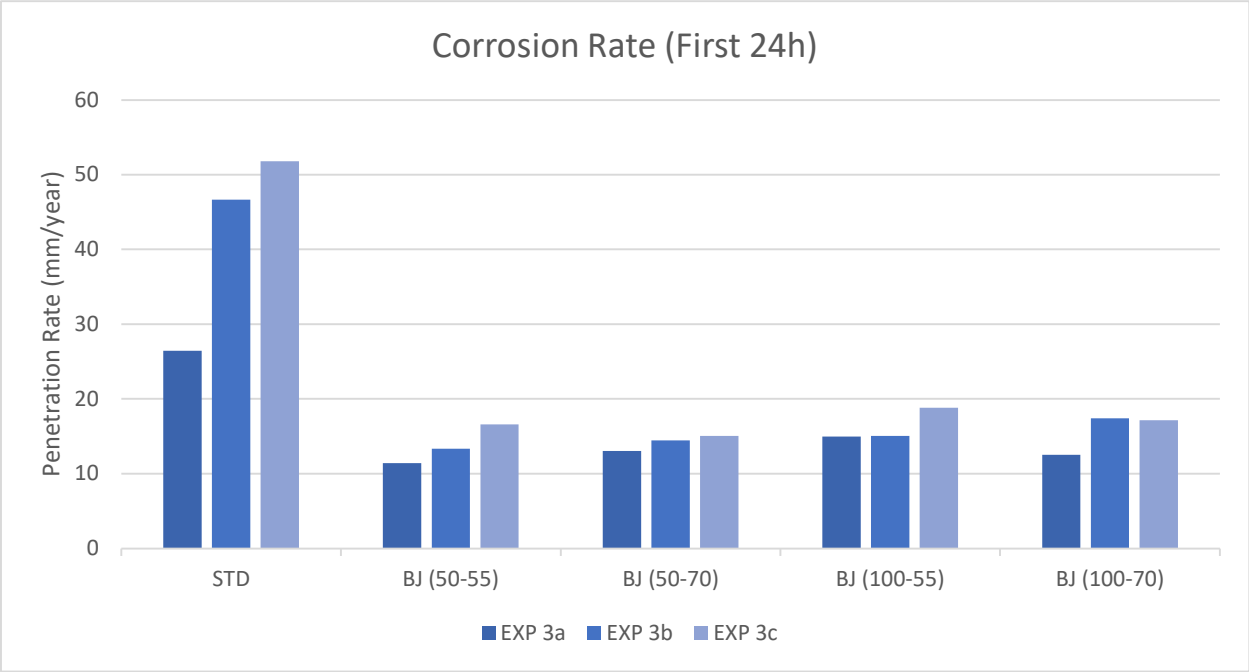

Graph 5 - Aggregated data from experiment n.3a, 3b and 3c - Corrosion at 24h

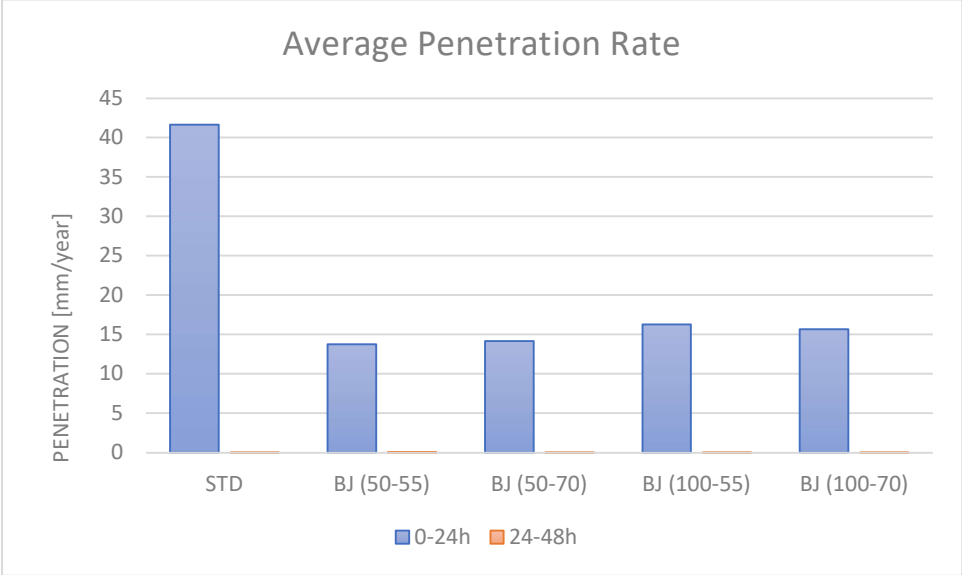

Graph 6– Experiment n.3a - Corrosion 24-48h

Table 11 - Experiment n.3 – Average corrosion 24-48h

Type of Specimen	Δ Mass / Surface Ratio [g/cm^2]		Penetration Rate [mm/yaer]	
	0-24h	24-48h	0-24h	24-48h
STD	0,090 ± 0,029	(2,72 ± 0,67) 10^{-5}	41,6 ± 13,4	0,013 ± 0,003
BJ1 (55BS 50LT)	0,029 ± 0,006	(1,62 ± 1,58) 10^{-4}	13,8 ± 2,6	0,077 ± 0,075

BJ2 (BS70 50LT)	0,030 ± 0,002	(4,68 ± 2,53) 10^{-5}	14,2 ± 1,0	0,022 ± 0,012
BJ3 (55BS 100LT)	0,035 ± 0,005	(7,76 ± 8,91) 10^{-5}	16,3 ± 2,2	0,037 ± 0,042
BJ4 (70BS 100LT)	0,033 ± 0,006	(5,64 ± 7,74) 10^{-5}	15,7 ± 2,8	0,027 ± 0,037

To explain the difference between the behavior at the second 24 hours in 2nd and 3rd tests, it is necessary to look at the differences between the operating procedures of the two experiments. There are three main differences:

- Sample preparation before the bath; ultrasonically degreased as sintered surfaces (2nd exp), polished surfaces (3rd exp).
- Dipping method; free in the solution (2nd exp), suspended by a Teflon thread (3rd exp).
- Treatment after the bath; water rinsing (2nd exp), ultrasonic bath in water and rinsing with water, ethanol, and acetone (3rd exp).

The main reason for the different behavior between the two experiments is probably the third step, accidentally creating a pickling and passivation process [42]. This is probably due to the crucial importance of cleaning and neutralization that must follow the acid bath. The quick rinsing of the second experiment must not have been sufficient to remove all traces of acid from the pits and pores. On the other hand, the complete passivation of the samples of the third experiment, thanks to the removal given by the pickling of the harmful precipitates from the surface (oxides and sulphides), gives a strong immunity for the second bath [59].

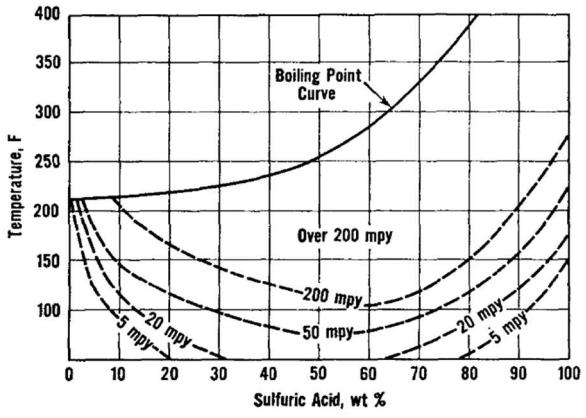

Figure 15 - Correlation between corrosion rate and temperatire and acid concentration [60].

From the weight loss experiments which compared BJ and STD, it is proven that BJ specimens have superior corrosion resistance in harsh sulfuric environment compared to STD specimens.

Comparing the corrosion rate obtained on STD with the data of 316L from literature [60], results are in line with the ambient temperature for 50% sulfuric acid (25 ° C = 77 ° F). Since the results obtained can therefore be considered reliable, it appears that the BJ technique provides higher resistance to corrosion than traditional metallurgical technique. This happens despite the presence of around 13% of ferritic δ phases [44], which should favor intergranular corrosion and pitting [61] in the surrounding Chromium depleted zone.

Through these experiments, it is also possible to verify the effect of the printing parameters. From these, it results that the variation of the binder saturation during printing does not bring considerable advantages, while instead there is an average increase of 12% in the rate of corrosion, doubling the layer thickness.

4.5.4 4th Experiment

The results show how weight loss still occurs abundantly in the hours following the first 24 hours, having a progressive increase in the corrosion rate. In addition to the progressing of corrosion, no plateau in rate is visible either. Graph 7, Graph 8 and Table 12.

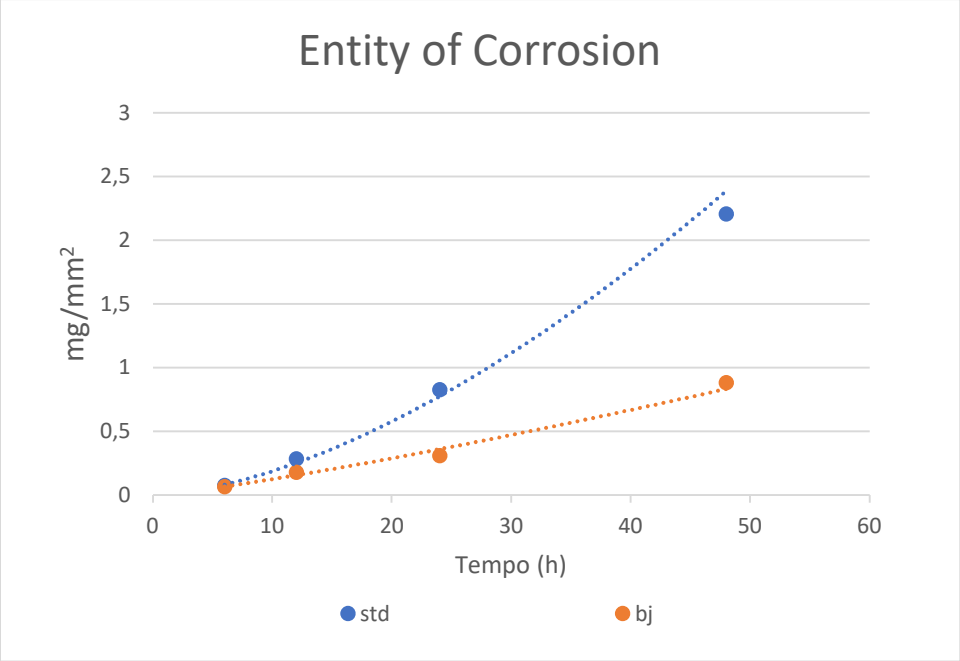

Graph 7 - Progress of corrosion at 6, 12, 24, 48 hours

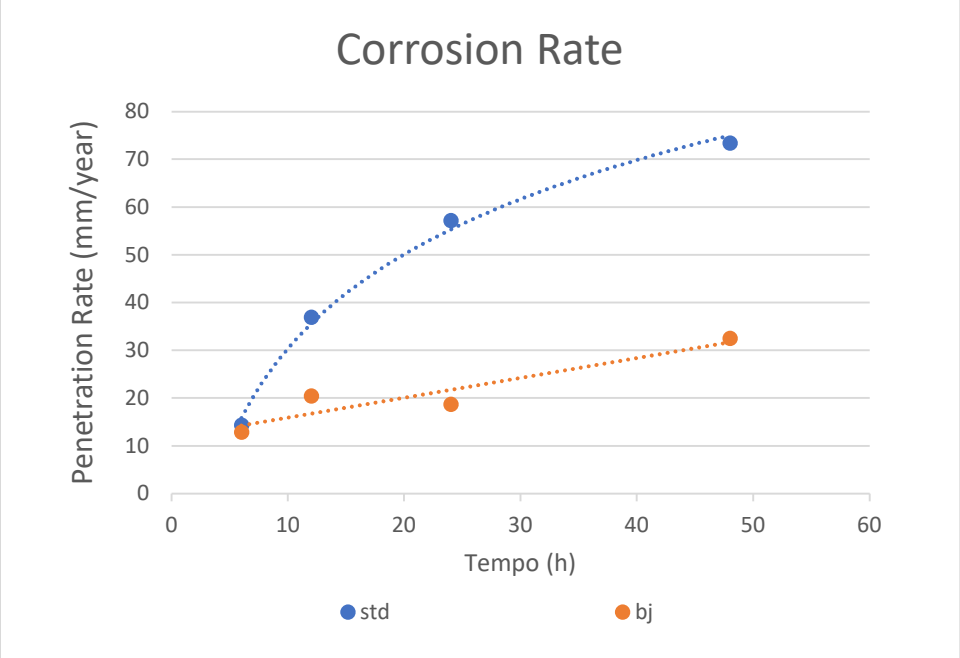

Graph 8 – Rate required for the specimens to corrode the difference in material from precedent time to specific time.

Table 12 – Corrosion data of the 4th experiment.

Type and immersion time of for each specimen	Δ Mass / Surface Ratio [mg/mm^2]	Penetration Rate [mm/yaer]
STD 6h	0,074	14,4
STD 12	0,282	36,9
STD 24	0,826	57,2
STD 48	2,205	73,4
BJ1 (55BS 50LT) 6h	0,065	12,9
BJ1 (55BS 50LT) 12h	0,177	20,4
BJ1 (55BS 50LT) 24h	0,310	18,7
BJ1 (55BS 50LT) 48h	0,883	32,5

4.6 Cyclic potentiodynamic polarization voltammetry

The STD specimen is sowing an anomalous behavior. Its results are unreliable, with illy reproducible graphs, while the other tests are significantly more consistent. Graph 9 and Table 13.

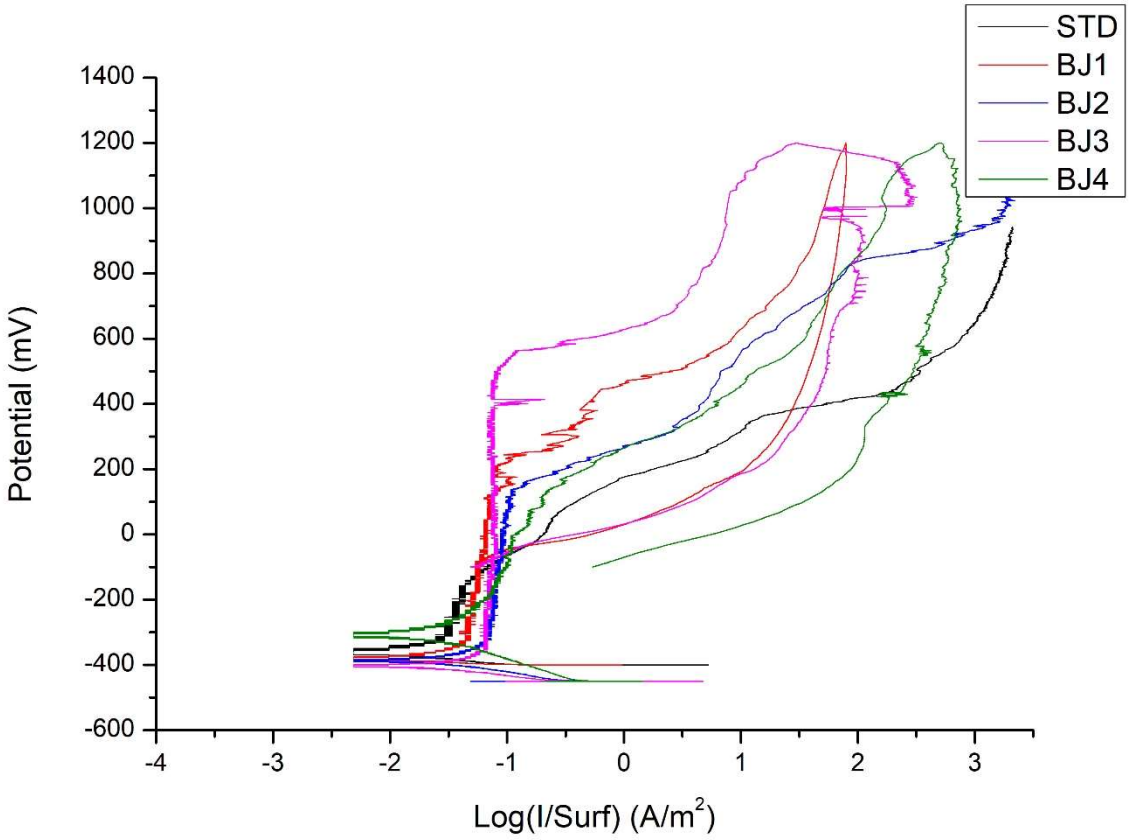

Graph 9 - Rappresentative polarization curves

Table 13 -Electrochemical results: corrosion potential (Ecorr), primary passivation potential (Ep), pitting potential (Epit), repassivation potential (Erep) and passive current density (ipass).

	E_{corr} (mV)	E_p (mV)	E_{pit} (mV)	E_{rep} (mV)	I_{pass} (A/m^2)
STD	-340 ±42	-310 ±14	-175 ±63	-120	0,036 ±0,02
BJ1	-350 ±42	-260 ±84	400 ±71	-70	0,073 ±0,001
BJ2	-370 ±21	-290 ±30	95 ±57	\	0,092 ±0,004
BJ3	-400	-330	500	-50	0,078
BJ4	-345 ±50	-250 ±71	240 ±113	-200	0,08 ±0,02

In the electrochemical evaluations an anomalous behavior of the STD specimen is highlighted in every test made, with a curve almost devoid of passive region. Therefore, analyzing the quantitative composition of the sample by means of a quantometer, a sulfur concentration, almost double the maximum limit for the alloy, is detected (the only parameter out of scale). Many studies in the literature [62] show that minimal variations in sulfur percentages have detrimental effect on pit initiation and growth [63] [64]. This is due to the precipitation of manganese sulphides at grain boundary, which strongly increase the susceptibility to pitting. Moreover, SEM images show prevailing elongated inclusions, which farther worsen the corrosion behavior. The effect on the polarization curves is similar to the one shown by the STD, with reduction in the pitting potential (Ep) up to an almost total disappearance of the passive area.

To evaluate the BJ results, the data from a different work with standard 316L specimen, tested under the same conditions of this study, are used [27]. The most significant effect is a lower pitting potential in the BJ specimens, on average lower than wrought 316L's (563mV vs SCE). These results are still acceptable considering how these potentials are fairly high for an environment rich in chlorides. The corrosion and passive region currents, and the corrosion potential are also slightly worsened compared to the standard 316L.

It is worth mentioning that all these parameters are heavily influenced by ambient factors, such as temperature. Since the two tests took place in different conditions, it is possible to assume that the differences between their parameters is lower than that measured, since the temperature must have negatively influenced them (with an average temperature of 30°C, higher than the conventional room temperature).

Furthermore, despite the large hysteresis of the BJ passivation curve, a repassivation is still achieved, defining a minimum perfect passivation interval. This is a good result, considering the extreme pitting the specimens were subjected to. At such current densities and potentials, the passive film degenerates and it is not always possible to return to a repassivation.

In addition, the few fluctuations of metastable pitting, visible only within the upper passive zone, suggest that the region of imperfect passivity should be limited to a high potential, in normal conditions.

Considering the printing parameters effect, a lower binder saturation results in higher pitting potential and a wider passivity range (+280mV E_p and 305mV wider region, on average), probably

due to a lower porosity, while the layer thickness does not seem to affect the electrochemical behavior.

4.7 SEM analysis of corroded specimens

The SEM images provide many critical hints and proves of the hypothesis made regarding the corrosion behavior.

Figure 16, Figure 17 and Figure 18 are representative images for each type of material analyzed, showing both cross section (CS) and outer surface (Surf), once subjected to corrosion by sulfuric acid. In order to better appreciate different aspect of the microstructure, the pictures were taken using secondary electrons (SE) and Backscattered Electrons (BSE).

With such a general prospective, only the most fundamental differences can be appreciated. It is difficult to find significant changes between different BJs, apart from a profile with more marked irregularities in BJ 3 and BJ 4 and a finer structure on BJ 2 external surface.

It is possible to obtain useful information by comparing Figure 16 and Figure 17 of BJ with Figure 18 of wrought 316L specimen. Here there are remarkable differences, with BJ's CSs showing pores and equiaxed precipitates, while that of the STD specimen shows linear ones, probably created by the mechanical processing of the piece, that has fragmented and scattered pre-existing precipitates. The surface appearance is also quite different, with much deeper and more regular cavities, clearly visible both in CS and on the outer surface.

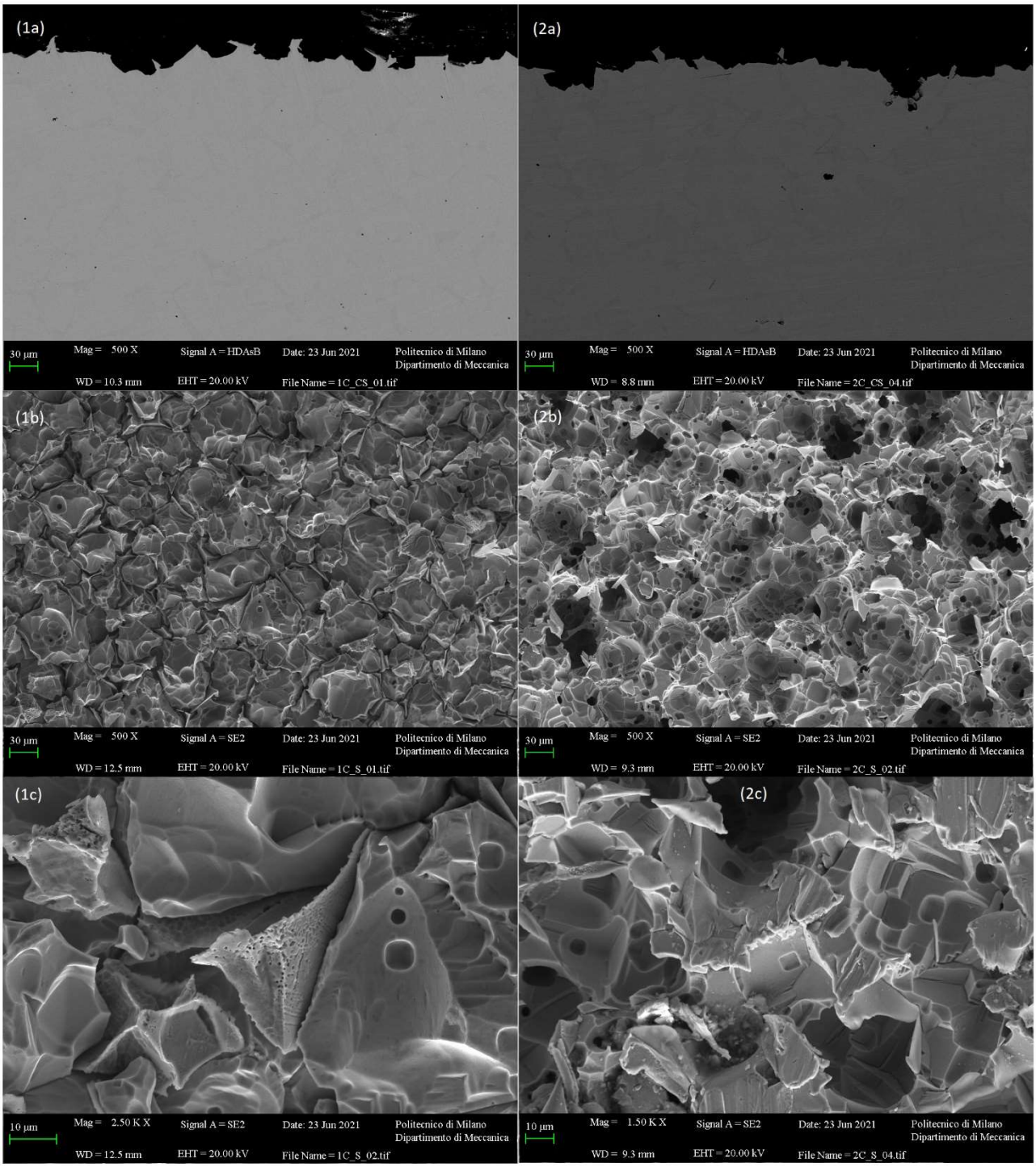

Figure 16 - SEM images of BJ1 and BJ2. (1a) CS of BJ1 with BSE; (1b) Surf of BJ1 with SE (1c) Surf of BJ1 magnified with SE; (2a) CS of BJ2 with BSE; (2b) Surf of BJ2 with SE; (2c) Surf of BJ2 magnified with SE;

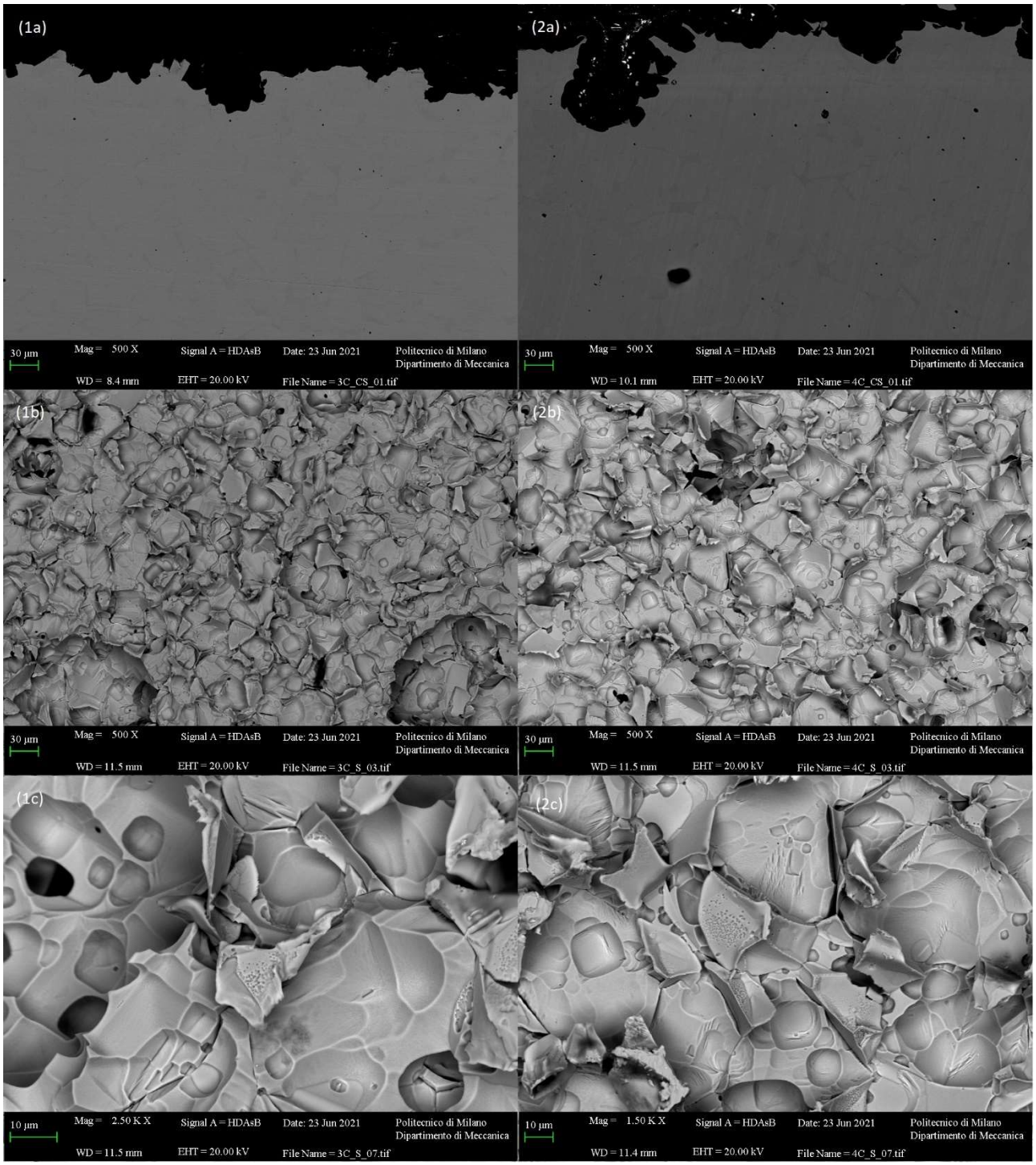

Figure 17 – SEM images of BJ3 and BJ4. (1a) CS of BJ3 with BSE; (1b) Surf of BJ3 with BSE (1c) Surf of BJ3 magnified with BSE; (2a) CS of BJ4 with BSE; (2b) Surf of BJ4 with BSE; (2c) Surf of BJ4 magnified with BSE;

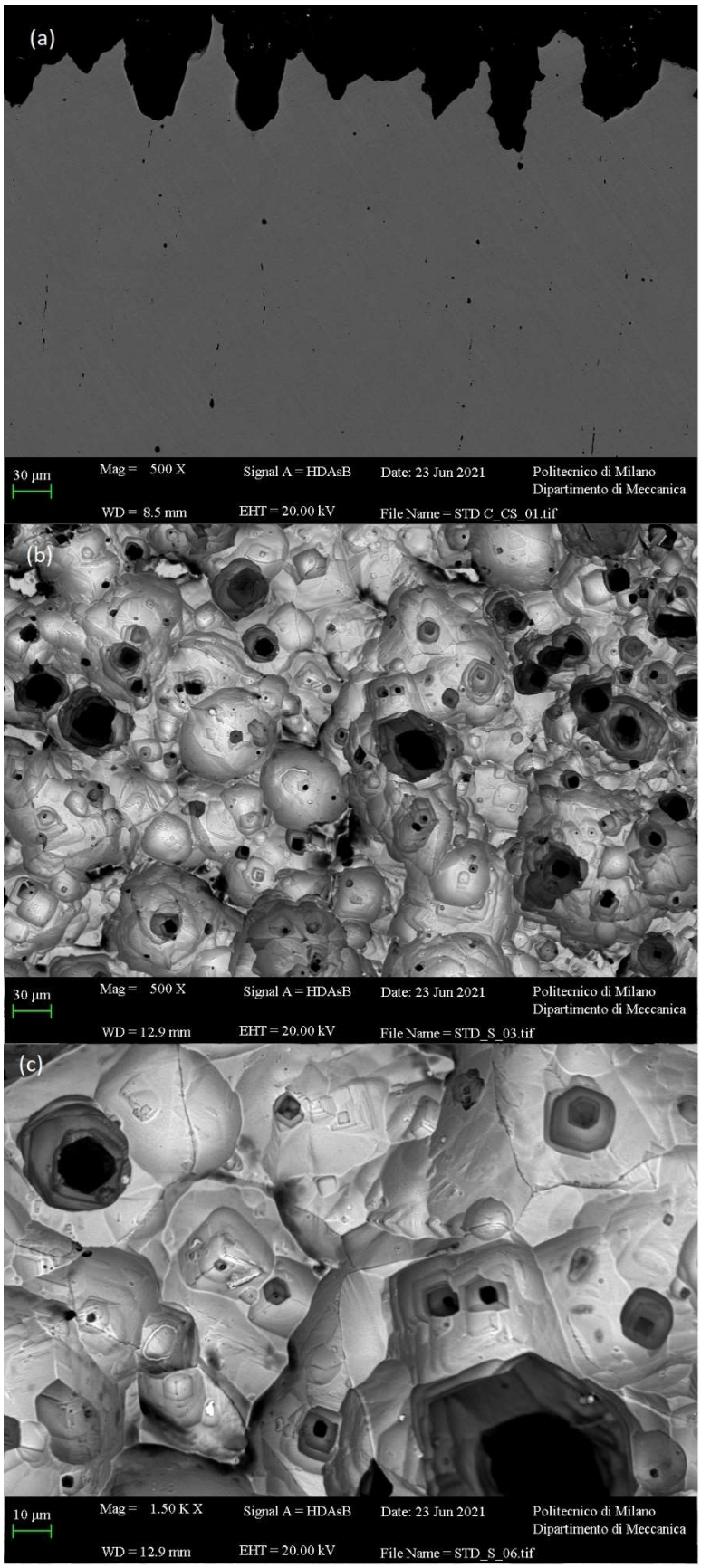

Figure 18 – SEM images of STD specimen. (a) CS of STD with BSE; (b) Surf of STD with BSE (c) Surf of STD magnified with BSE;

As shown in most cross-section images, and even better in Figure 19, there are two phases inside the BJ specimens: γ austenite and δ ferrite on the grain boundary. The standard 316L is instead composed of a single phase, as shown in Figure 18a.

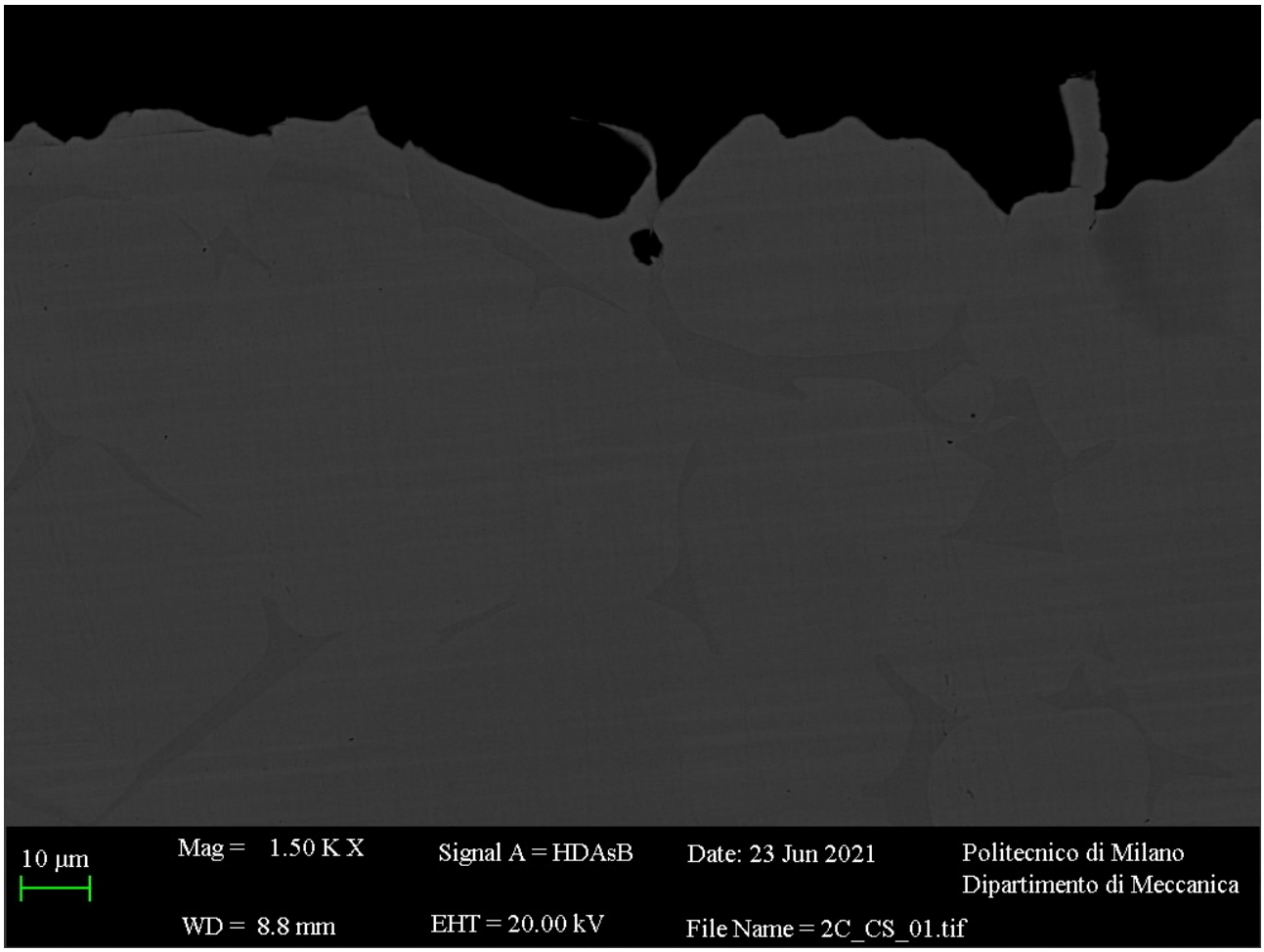

Figure 19 – SEM CS of BJ specimen using BSE, with clear display of both phases. The large matrix-like grains of austenite γ contrast against the darker δ ferrite with sharper shapes due to its growth at the grain boundary.

The concentration of chromium in the δ phase is higher, thanks to the greater ability to accommodate the chromium atoms within the BCC crystal lattice of the ferrite (Figure 20a). This chromium was extracted from the area surrounding the ferrite, leaving it depleted and therefore more easily subjected to corrosion.

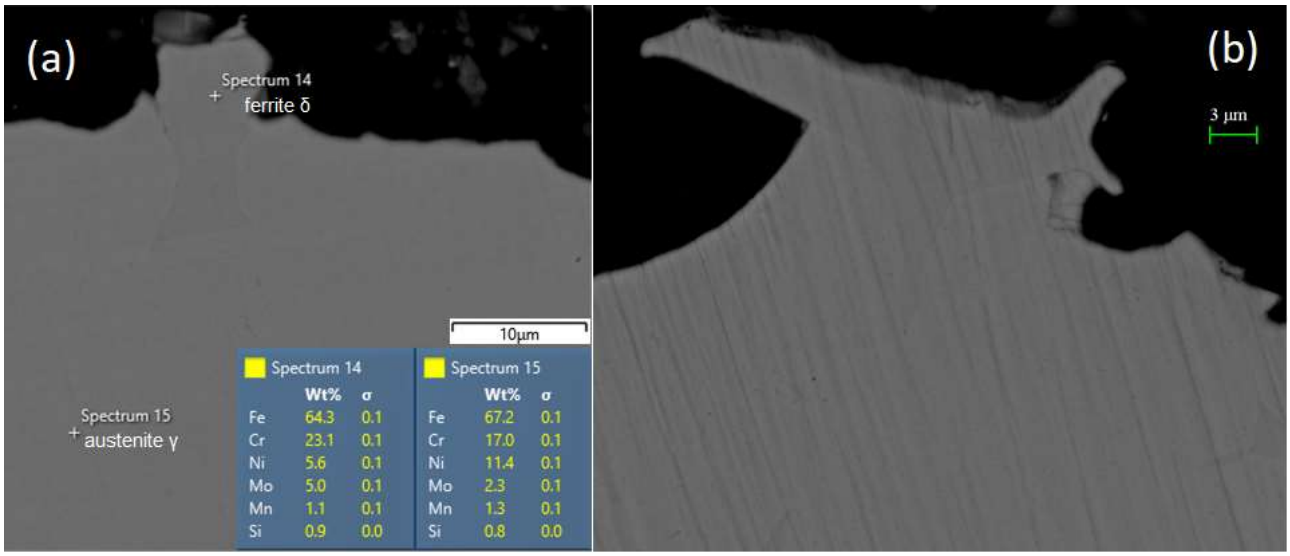

Figure 20 – SEM immages of BJ CSs. (a) δ and γ phase composition. (b) attack on the depleted γ zone adjacent a δ grain.

Focusing the attention on magnified regions of the external surface, it is possible to observe effects of austenite impoverishment. Figure 20b shows how the δ phases that remain exposed on the surface are significantly less attacked by corrosion, while the surrounding areas wear out much more quickly.

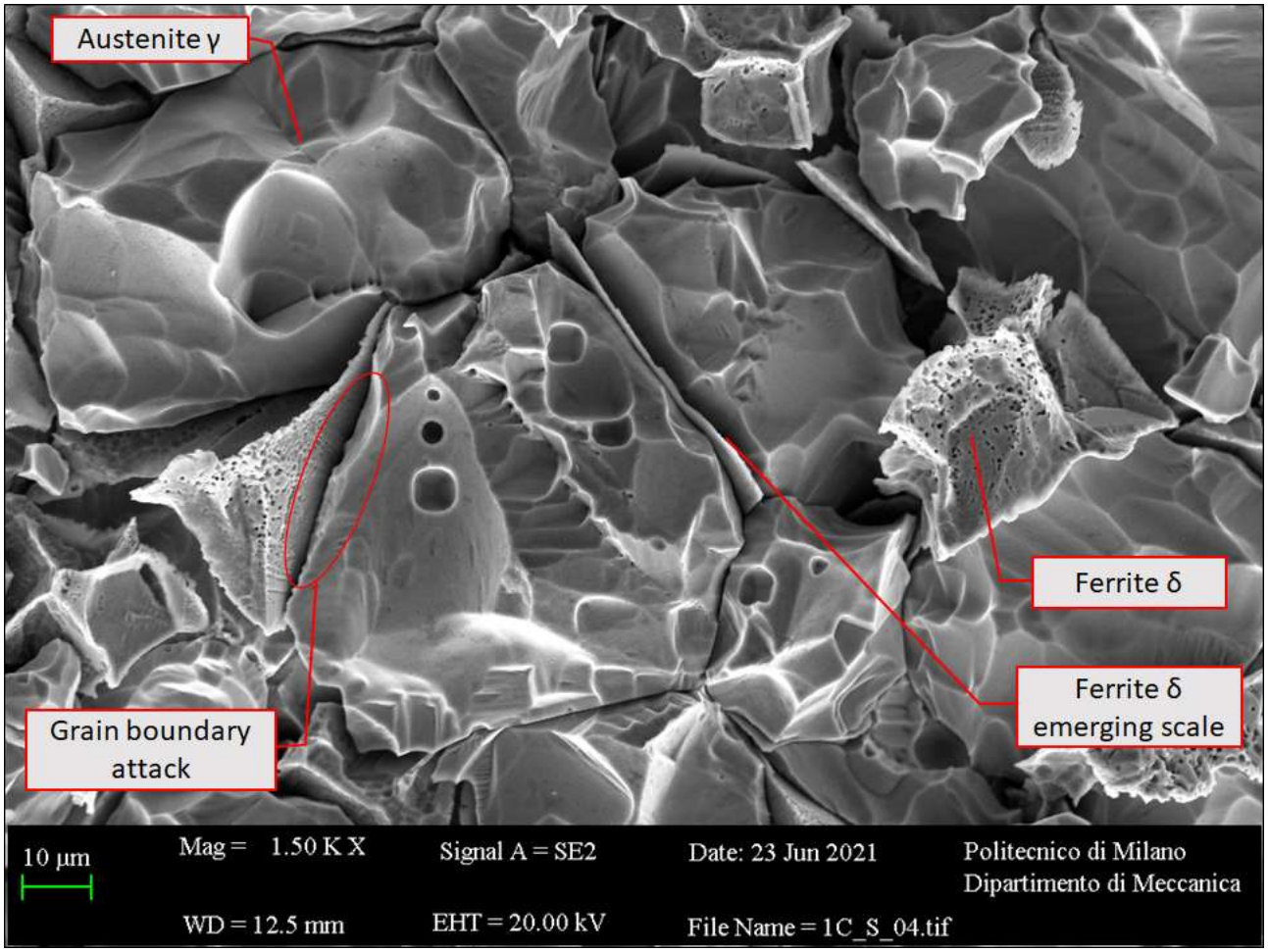

Figure 21 – SEM immage of corroded BJ surface.

Also observing the outer surface, strong corrosion at the grain boundary, around the δ ferrite flakes, is shown (Figure 21). It is also possible to see a different type of corrosion between the zones, with the δ phase scales that undergo pitting before being separated from the γ matrix, which instead seems to undergo mainly intergranular and generalized corrosion, with rarer pits.

In Figure 22 is possible to observe the cross section of some pitting attacks. On the left the pitting is starting within the depleted zone around a ferrite scale and on the right a growing cluster of pits.

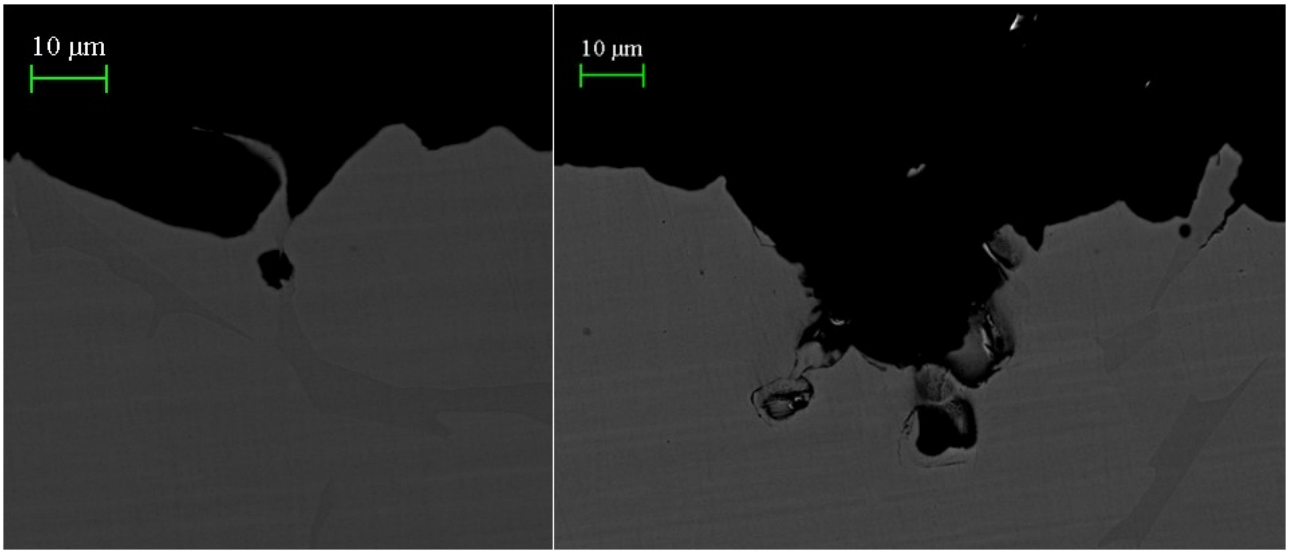

Figure 22 – Starting of a pit within the Cr depleted γ zone, around a ferrite scale (left); Propagation of a cluster of pits (right).

In all the cross-sections images, pores and inclusions are visible as black spots. In particular, pores and chromium carbides are present in the BJ samples, with some rare oxides, while in the STD specimen manganese sulphides are more prevalent (Figure 23, left).

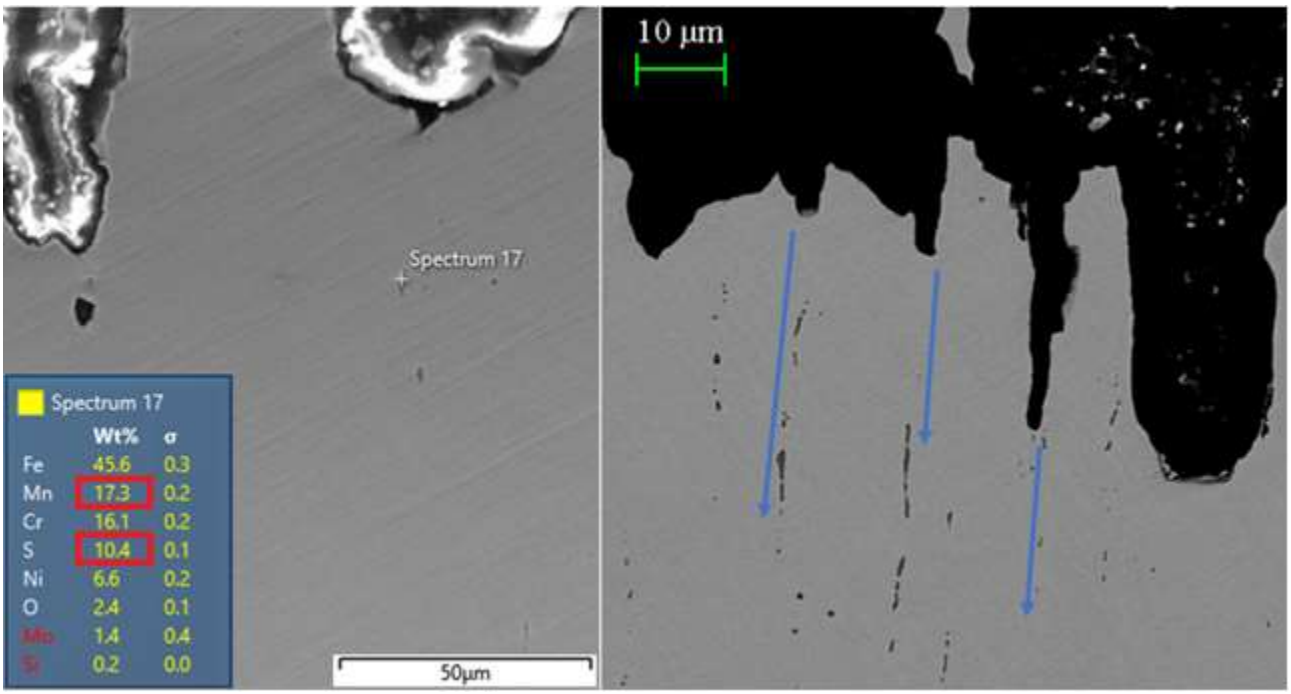

Figure 23 – Measurement of the composition of a small area comprising a manganese sulfide precipitate in the STD specimen (left); Alignment of surface corrosion pits with elongated sulfide precipitations (right).

In Figure 23 (right) the linear nature of these precipitates is displayed, and how corrosion penetrates following them as preferential paths, giving a porous aspect to the surface, due to the pit-like shape of this corrosion (Figure 24).

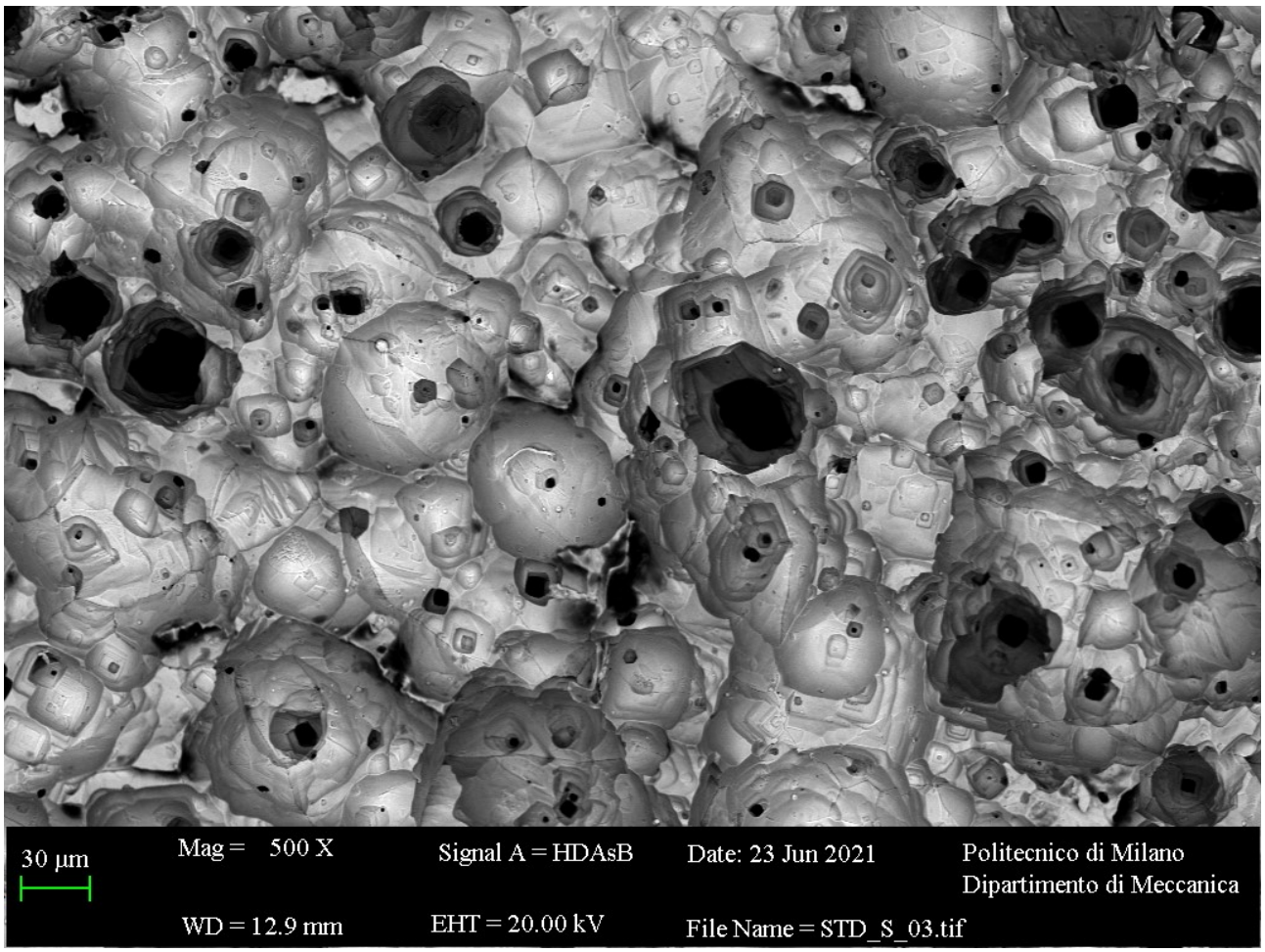

Figure 24 – SEM image of STD external surface after corrosion.

Comparing the data presented in Figure 25 it is possible to appreciate the homogeneity in composition content, especially for Cr, showing no gradient from the surface to bulk.

Figure 25 – SEM image of BJ CS, with EDX analysis of composition at different depths.

4.8 Surface roughness

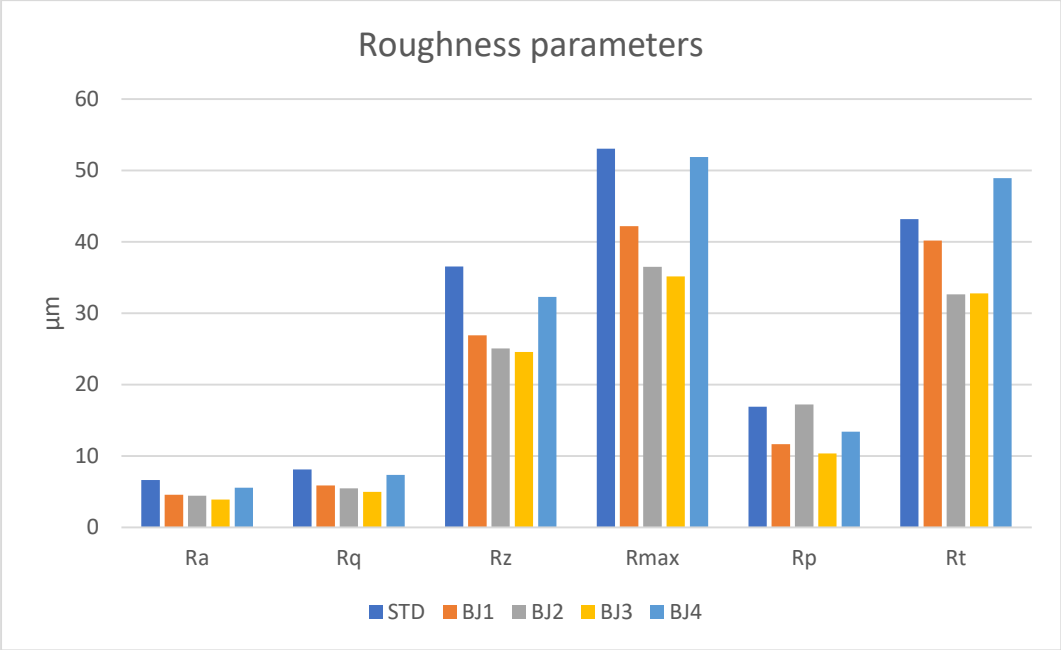

Graph 10 - Average surface = ideal flat surface positioned at the average height of all peaks and all valleys; Ra = Average distance of the real surface from the average surface; Rq = Mean square deviation from average surface; Rz = Average distance of the real

surface from the average surface, calculated only on the 5 maxima and minima; Rmax = Max peak-valley distance; Rp = Max peak height from average surface; Rt = Average distance between max valley and max peak.

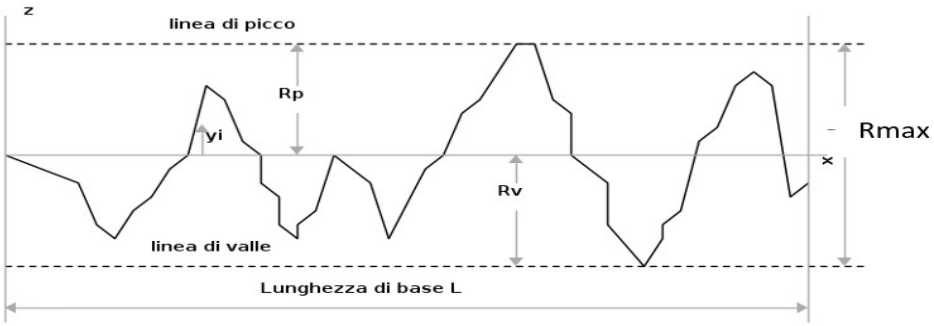

Figure 26 – Schematic rappresentation of roughness parameters.

No clear correlation seems to exist between the extent or rate of corrosion and the final roughness (Graph 11). This is more evident by excluding the STD sample which, having a different microstructure and corrosion mechanism, alters the correlation curve. In fact, part (b) shows absence of significance.

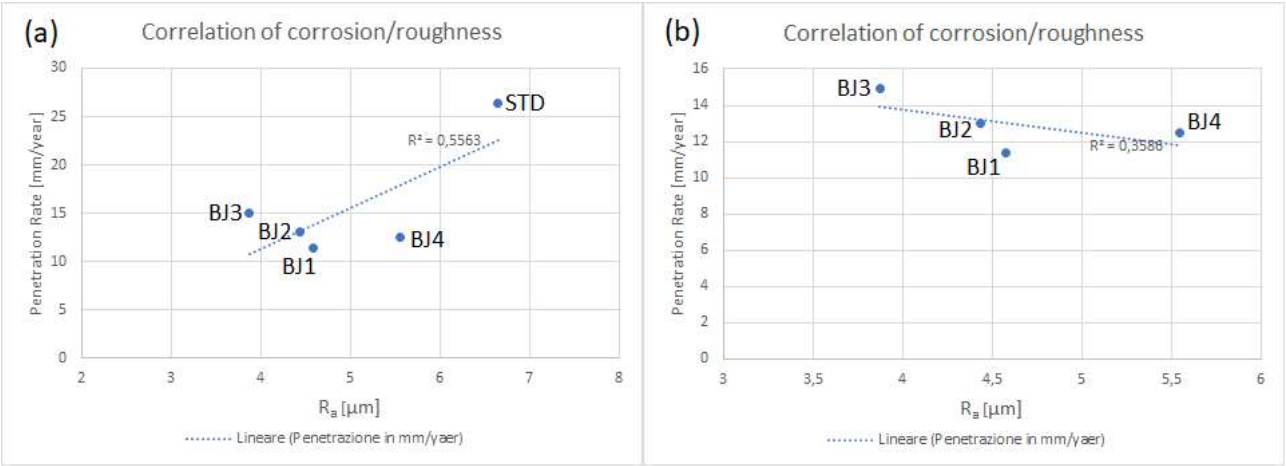

Graph 11 – (a) Linear correlation of all specimens; (b) Linear correlation excluding STD.

5. Conclusions

In the present thesis, processing parameters on the microstructure, mechanical behavior, and corrosion resistance of 316L stainless steel produced by Binder Jetting were investigate.

The samples produced by BJ technique were created using four sets of parameters, varying the two main printing parameters, Layer Thickness (LT) and Binder Saturation (BS). The tested specimens are therefore BJ1 (55BS 50LT), BJ2 (70BS 50LT), BJ3 (55BS 100LT) and BJ4 (70BS 100LT).

The debinding heat treatment was performed at 470°C in argon atmosphere, even though the absence of an oxidating atmosphere determined the retention of carbonaceous species in the specimens and a subsequent carbon enrichment, leading the overall carbon content from 0.03 wt% to 0.13 wt%. In addition, after the sintering treatment carried out in vacuum at 1360°C, specimens underwent a phase transition that lead to the formation of γ phase with intergranular δ phase at room temperature, and this event is likely attributed to the excess of carbon derived from the binder.

Inhomogeneities in both microstructure and mechanical behavior are observed, by increasing the binder saturation, especially when high values of layer thickness are set. This is due to the higher presence of residual carbon resulting in the debinded samples and poor powder packing.

The intergranular corrosion and pitting resistance are also affected by oxides and carbides inclusion. To understand the effect on corrosion behavior of the BJ printed specimens, a comparison was made with 316L steel produced by traditional techniques, and another among BJ specimens obtained by varying printing parameters.

BJ showed a distinctly higher corrosion resistance to intergranular corrosion during the weight loss tests. BJ (50-55) suffered 68% less corrosion than wrought 316L. Layer thickness has also been identified as a useful parameter to influence this type of corrosion, with higher corrosion (+12%) for thicker layers. Binder saturation gives inconsistent results.

During the cyclic potentiodynamic polarization experiments, BJ specimens show comparable resistance with respect to standard 316L SS. Binder saturation is the printing parameter identified as the most significant to improve pitting corrosion resistance ad passivity range, with positive effects for lower concentrations.

In addition, results suggest that a pickling and passivation treatment on this metal may be possible, regardless of the manufacturing technique. With such treatment corrosion resistance would be greatly enhanced, but further tests are required to verify this possibility.

6. Abbreviation

AD	Additive Manufacturing
ASTM	American Standard Testing Material
BJ	Binder Jetting
BJ3DP	Binder Jetting 3-Dimensional Printing
BS	Binder Saturation
BSE	Backscattered Electrons
CAD	Computer Assisted Design
CPP	Cyclic Potentiodynamic Polarization
CPV	Cyclic Potentiodynamic polarization Voltammetry
CS	Cross Section
DED	Directed Energy Deposition
DMLS	Direct Metal Laser Sintering
EBM	Electron Beam Melting
HAZ	Heat Affected Zone
HV	Vickers hardness
LT	Layer Thickness
PBF	Powder Bed Fusion
SE	Secondary Electrons
SLA	Stereo Lithography Appearance
SLM	Selective Laser Melting
SLS	Selective Laser Sintering
SS	Stainless Steel
STD	Standard
Surf	Outer surface
CPV	Cyclic Potentiodynamic polarization Voltammetry
CPP	Cyclic Potentiodynamic Polarization

7. References

[1] J.-P. Kruth, M. Leu e T. Nakagawa, «Progress in Additive Manufacturing and Rapid Prototyping,» *CIRP Ann,* pp. 525-540, 1998.

[2] B. Mueller, «Additive Manufacturing Technologies—Rapid Prototyping to Direct Digital Manufacturing.,» *Assem. Autom.,* n. 32, pp. 151-154, 2012.

[3] W. Gao, Y. Zhang, D. Ramanujan, K. Ramani, Y. Chen, C. Williams, C. Wang, Y. Shin e S. Zhang, «The status, challenges, and future of additive manufacturing in engineering.,» *Comput. Des.,* n. 69, pp. 65-89, 2015.

[4] N. Guo e M. Leu, «Additive manufacturing: Technology, applications and research needs,» *Front. Mech. Eng,* n. 8, pp. 2015-243, 2013.

[5] C. M. Savolainen J, «How additive manufacturing technology changes business models? Review,» *Additive Manufacturing,* 2020.

[6] D. Bourell, J. Kruth, M. Leu, G. Levy, D. Rosen, A. Beese e A. Clare, «Materials for additive manufacturing.,» *CIRP Ann,* n. 66, p. 659–681, 2017.

[7] Standard, ISO/ASTM 52900 - Standard Terminology for Additive Manufacturing – General Principles, vol. Part 1: Terminology, West Con-shohocken, PA.: ASTM, 2005.

[8] P. Gokuldoss, S. Kolla e J. Eckert, «Additive Manufacturing Processes: Selective Laser Melting, Electron Beam Melting and Binder JettingSelection Guidelines,» *Materials ,* n. 10, 2007.

[9] B. Conner, G. Manogharan, A. Martof, L. Rodomsky, C. Rodomsky, D. Jordan e J. Limperos, «Making sense of 3-D printing: Creating a map of additive manufacturing products and services.,» *Addit. Manuf.,* n. 1, p. 64–76., 2014.

[10] B. Stucker, «Additive manufacturing technologies: Technology introduction and business implications.,» *National Academies Press,* pp. 19-21, 2012.

[11] S. Mirzababaei e S. Pasebani, «A Review on Binder Jet Additive Manufacturing of 316L Stainless Steel,» *Journal of Manufacturing and Materials Processing,* 2019.

[12] T. DebRoy, H. Wei, J. Zuback, T. Mukherjee, J. Elmer e J. Milewski, «Additive manufacturing of metallic components.Process, structure and properties.,» *Prog Mater Sci,* vol. 92, pp. 112-224, 2018.

[13] Y. Zhang, X. Cao, P. Wanjara e M. Medraj, «Oxide Films in Laser Additive Manufactured Inconel 718,» *Acta Materialia,* p. 6562–6576, 2013.

[14] B. Zhang, Y. Li e Q. Bai, «Defect Formation Mechanisms in Selective Laser Melting: A Review,» *Chin. J. Mech. Eng,* n. 30, p. 515–527, 2017.

[15] M. Nastac e R. Klein, «ExOne, I. Microstructure and mechanical properties comparison of 316L parts,» in *In Proceedings of the 28th Annual International Solid Freeform Fabrication Symposium—An Additive Manufacturing Conference,*, Austin TX, 2017.

[16] M. Ziętala, T. Durejko, M. Polanski, I. Kunce, T. Płociński, W. Zieliński, M. Łazińska, W. Stępniowski, T. Czujko, K. Kurzydłowski e Z. Bojar, «The microstructure, mechanical properties and corrosion resistance of 316L stainless steel fabricated using laser engineered net shaping,» *Materials Science and Engineering,* p. 667, 2016.

[17] E. Sachs, M. Cima, P. Williams, Brancazio.D e J. Cornie, «Dimensional Printing - Rapid Tooling and Prototypes Directly from a Cad Model,» *J. Eng. Ind. Asme.,* n. 114, p. 481–488., 1992.

[18] I. Gibson, D. Rosen e B. Stucker, In Additive Manufacturing Technologies: 3D Printing, Rapid Prototyping, and Direct Digital Manufacturing;, New York, NY, USA: Springer, 2015; pp. 205–218., pp. 205-218.

[19] A. Mostafaei, A. M. Elliott, J. E. Barnes, F. Li e W. Tan, «Binder jet 3D printing—Process parameters, materials, properties, modeling, and challenges,» *Progress in Materials Science,* vol. 119, 2021.

[20] K. Rego, J. Yeom e P. Kwon, «Additively Manufactured Full-Density Stainless Steel 316L with Binder Jet Printing,» in *In Proceedings of the ASME 2018 13th International Manufacturing Science and Engineering*, College Station, TX, USA, 2018.

[21] T. Do, P. Kwon e C. Shin, «Process development toward full-density stainless steel parts with binder jetting printing,» *Int. J. Mach. Tools Manuf,* n. 121, pp. 50-60, 2017.

[22] H. Juan, «Effect of Temperature Ratio (ts/tm) and Time on the Sintering Behavior of Metallic 316l Stainless Steel Coupons Coupons Produced Using Jet-Binder Technology,» Master's Thesis, University of Pittsburgh, Pittsburgh, PA, USA,, 2017.

[23] M. Ziaee e N. Crane, « Binder jetting: A review of process, materials, and methods.,» *Addit. Manuf.,* n. 28, p. 781–801, 2019.

[24] C. W. Kovach, «High performance stainless stell,» *Nickel Institute,* pp. 12-22, 2018.

[25] B. Voronenko, «Austenitic-ferritic stainless steels: A state-of-the-art review,» *Met Sci Heat Trea,* n. 39, p. 428–437, 1997.

[26] Y. F. Cheng, J. Bullerwell e F. R. Steward, «Electrochemical Investigation of the Corrosion Behavior of Chromium-Modified Carbon Steels in Water,» *Electrochim. Acta,* vol. 48, p. 1521–1530, 2003.

[27] M. Atapour, «Corrosion of Binder Jetting Additively Manufactured 316L Stainless Steel of Different Surface Finish 2020,» *J. Electrochem. Soc,* n. 167, 2020.

[28] M. Ryan, D. Williams e R. Chater, «Stainless-steel corrosion and MnS inclusions.,» *Nature,* n. 424, p. 390, 2003.

[29] T. Bellezze, G. Giuliani e G. Roventi, «Study of stainless steels corrosion in a strong acid mixture. Part 1: cyclic potentiodynamic polarization curves examined by means of an analytical method,» *Corrosion Science,* vol. 130, 2018.

[30] S. Esmailzadeh, H. Sarlak e M. Aliofkhazraei, «Interpretation of ciclyc potentiodynamic polarization test results for study of corrosion behavior of metal: a review,» *Protection of metals and Physical chemistry of surfaces,* vol. 54, pp. 976-989, 2018.

[31] D. Brandon e W. Kaplan, Microstructural Caharacterization of Materials, Israel: Jhon Wiley & Sons, 2008.

[32] M. E. A. Del Zoppo, «Lectures of "Surface analysis and characterization",» 2018.

[33] G. Sander, J. Tan, P. Balan, O. Gharbi, D. Feenstra e L. Singer, «Corrosion of Additively Manufactured Alloys: A Review,» *CORROSION,* vol. 74, pp. 1318-1350, 2017.

[34] C. P. Allen, «Investigation of the Structure and Corrosive Properties of Additively Manufactured Stainless Steel 316L by Binder Jetting and Supersolidus Liquid Phase Sintering,» *Master Thesis of Drexel University PA. USA,* 2016.

[35] Q. Chao, V. Cruz, S. Thomas, N. Birbilis, P. Collins, A. Taylor, P. Hodgson e D. Fabijanic, «On the enhanced corrosion resistance of a selective laser melted austenitic stainless steel,» *Scr.Mater.,* vol. 141, p. 94–98, 2017.

[36] X. Wang, K. Färnlund, M. Atapour e Y. Hedberg, «Corrosion and metal release investigations of selective laser melted 316L stainless steel in a synthetic physiological fluid containing proteins and in diluted hydrochloric acid,» *Electrochimica Acta,* vol. 354, n. 13678, 2020.

[37] R. I. Revilla, M. Van Calster, M. Raes, G. Arroud, F. Andreatta, L. Pyl, P. Guillaume e I. De Graeve, «Microstructure and corrosion behavior of 316L stainless steel prepared using different additive manufacturing methods: A comparative study bringing insights into the impact of microstructure on their passivity,» *Corrosion Science,* vol. 176, n. 108914, 2020.

[38] G. Ko, W. Kim, K. Kwon e T.-K. Lee, «The Corrosion of Stainless Steel Made by Additive Manufacturing: A Review,» *Metals,* vol. 3, p. 516, 2021.

[39] J. Trelewicz, G. Halada, O. Donaldson e G. Manogharan, «Microstructure and corrosion resistance of laser additively manufactured 316L stainless steel,» *JOM,* vol. 68, p. 820–859, 2016.

[40] C. Örnek, «Additive manufacturing – a general corrosion,» *Corrosion Engineering, Science and Technology,* vol. 7, pp. 531-535, 2018.

[41] T. Do, T. Bauder, H. Suen, R. K. J. Yeom e K. P. , «Additively Manufactured Full-Density Stainless Steel 316L With Binder Jet Printing,» vol. 1, 2018.

[42] P. Pedeferri, Corrosion Science and Engineering, Cham, Switzerland: Springer, 2018.

[43] T. Do, K. P. e S. C. , «Process development toward full-density stainless steel parts with binder jetting printing,» *Int. J. Mach. Tools Manuf.,* vol. 121, pp. 50-60, 2017.

[44] N. Lecis, R. Beltrami e M. Mariani, «Binder jetting 3D printing of 316 stainless steel: influence of process parameters on microstructural and mechanical properties,» *La Metallurgia Italiana,* 2021.

[45] B. Verlee, T. Dormal e J. Lecomte-Beckers, «Density and porosity control of sintered 316L stainless steel parts produced by additive manufacturing,» *Powder Metall,* vol. 55, pp. 260-267, 2012.

[46] P. Nandwana, R. Kannan e D. Siddel, «Microstructure evolution during binder jet additive manufacturing of H13 tool steel.,» *Addit. Manuf,* vol. 36, 2020.

[47] F. Buffington, «Self diffusion in iron,» *Acta Metall.,* vol. 9, p. 434–439, 1961.

[48] H. Shih, Corrosion Resistence, Croatia: inThec, 2012.

[49] J. Burke, «Role of Grain Boundaries in Sintering,» *J. Am. Ceram. Soc,* Vol. %1 di %280-85, p. 40, 1957.

[50] A. Kumar, Y. Bai, A. Eklund e C. Williams, « Effects of Hot Isostatic Pressing on Copper Parts Fabricated via Binder Jetting,,» *45th Sme North Am. Manuf. Res. Conf,* vol. 45, p. 935–944, 2017.

[51] E. Mendoza Jimenez, D. S. Ding, L., A. Joshi, A. Singh, B. Reeja-Jayan e J. Beuth, «Parametric analysis to quantify process input influence on the printed densities of binder jetted alumina ceramics.,» *Addit. Manuf. ,* vol. 30, 2019.

[52] M. Zago, N. Lecis, M. Vedani e I. Cristofolini, « Dimensional and geometrical precision of parts produced by binder jetting process as affected by the anisotropic shrinkage on sintering.,» *Addit. Manuf.,* vol. 43, 2021.

[53] R. Warren, «Microstructural development during the liquid-phase sintering of two-phase alloys, with special reference to the NbC/Co system,» *J. Mater. Sc.,* vol. 3, pp. 471-485, 1698.

[54] Z. Sun, X. Tan, S. Tor e W. . Yeong, « Selective laser melting of stainless steel 316L with low porosity and high build rates.,» *Mater. Des.,* pp. 197-204, 2016.

[55] M. Hamidi, W. Harun, N. Khalil e M. Samykano, «Microstructural comparison and mechanical properties of stainless steel 316L fabricated by selective laser melting and metal injection moulding processes.,» *Int. J. Manuf. Technol. Manag,* vol. 33, pp. 76-87, 2019.

[56] R. Casati, J. Lemke e M. Vedani, « Microstructure and Fracture Behavior of 316L Austenitic Stainless Steel Produced by Selective Laser Melting.,» *J. Mater. Sci. Technol.,* vol. 32, pp. 738-744, 2016.

[57] H. Alsalla, C. Smith e L. Hao, « Effect of build orientation on the surface quality, microstructure and mechanical properties of selective laser melting 316L stainless steel.,» *Rapid Prototyp. J.,* vol. 24, pp. 9-17, 2018.

[58] «ASTM International, A276/A276M-17 Standard Specification for Stainless Steel Bars and Shapes,» *ASTM Int.,* 2017.

[59] M. Boniardi e V. Boneschi, «Decapaggio e passivazione degli acciai industriali,» 2005. [Online]. Available: www.meccanicanews.com.

[60] INCO, «Corrosion Rsistence of The Austenite Chromium Nikel Stainless Seel in Chemical Environment,» The international Nickel Company, New York (US), 1963.

[61] T. Bellezze, G. Giuliani, G. Roventi, R. :. A. F. Fratesi e L. Fedrizzi, «Corrosion behaviour of austenitic and duplex stainless steels in an industrial strongly acidic solution,» *2016,* vol. 67, p. 831–838, Mater. Corros.

[62] N. Hara, K. Hirabayashi, Y. Sugawara e I. Muto, «Improvement of Pitting Corrosion Resistance of Type 316L Stainless Steel by Potentiostatic Removal of Surface MnS Inclusions,» *International Journal of Corrosion,* 2012.

[63] G. Eklund, «Inizitaion of pitting at sulfide inclusions in stainless steel,» *Journal of Electrochemica Society,* vol. 121, n. 4, pp. 467-473, 1974.

[64] M. Baker e E. Castle, «The initation of pitting corrosion at MnS inclusions,» *Corrosion Science,* vol. 34, n. 4, pp. 667-682, 1993.

[65] A. A.M. Elliott, A. Momen, M. Benedict e J. Kiggans, « A Method for Measuring Powder Bed Density in Binder Jet Additive Manufacturing Process and the Powder Feedstock Characteristics Influencing the Powder Bed Density,» in *Int. Mech. Eng. Congr. Expo*, 2016.

[66] Y. Mao, J. Li, W. Li, D. Cai e Q. Wei, «Binder jetting additive manufacturing of 316L stainless-steel green parts with high strength and low binder content: Binder preparation and process optimization,» *J. Mater. Process. Technol,* vol. 291, 2021.

[67] F. Buffington, K. Hirano e M. Cohen, «Self diffusion in iron,» vol. 9, p. 434–439, 1961.

[68] P. Nandwana, R. Kannan e D. Siddel, «Microstructure evolution during binder jet additive manufacturing of H13 tool steel,,» *Addit. Manuf.,* vol. 36, 2020.

[69] B. Verlee, T. Dormal e J. Lecomte-Beckers, «Density and porosity control of sintered 316L stainless steel parts produced by additive manufacturing,» *Powder Metall. ,* vol. 55, p. 260–267, 2012.